ISSN: 2639-0108

Review Article

Advances in Theoretical & Computational Physics

Alpha-buckets in High Energy Electron Storage Rings (Review of Existing Experiments and Feasibility Studies for Future Developments)

A. Papash*, M. Brosi, P. Schreiber, T. Boltz, N. Smale, A.-S. Müller, R. Ruprecht, M. Schuh

Karlsruhe Institute of Technology, P.O. Box 3640 Karlsruhe 76012 Germany

***Corresponding author**
A.Papash, Karlsruhe Institute of Technology, P.O. Box 3640 Karlsruhe 76012 Germany.

Submitted: 05 Apr 2021; **Accepted:** 12 Apr 2021; **Published:** 29 Apr 2021

Citation: *A. Papash, M. Brosi, P. Schreiber, T. Boltz, N. Smale, et al. (2021). Alpha-buckets in High Energy Electron Storage Rings (Review of Existing Experiments and Feasibility Studies for Future Developments). Adv Theo Comp Phy, 4(2), 148-178.*

Abstract

Electron storage rings operating at high energies have proven to be invaluable source of synchrotron radiation. Two and even three simultaneous beams of particles have been observed at different light source facilities worldwide. So called alpha-buckets were studied at Metrological Light Source (MLS) in Berlin (Germany), SOLEIL facility in France, DIAMOND light source in UK, NSLS ring in Brookhaven (USA). It is widely recognized that alpha buckets are general phenomena which is not restricted to a certain storage ring. However, earlier measurements showed essential limitations on parameters of alpha-buckets, strong dependence on high order (sextupole and octupoles) magnetic field imperfections and associated fast decay of electron current as well as reduced life time. Also a rising relevance of high order non-linear longitudinal beam dynamics is associated with new generation of diffraction limited light sources (DLSR) approaches, which all suffer nonlinear momentum compaction factor. A large variety of future generation electron synchrotrons require a comprehensive investigation of the physical processes involved into the operation of such rings.

In this paper, we present review of high order non-linear longitudinal beam dynamics based on the longitudinal equations of motion and Hamiltonian expanded to a high order of the momentum compaction factor.

Roots of the third order equation with a free term are derived in a form suitable for analytical estimations. The momentum independent term of orbit lengthening due to particle transverse excursions is estimated and taken into account. The results from simulations were benchmarked against existing experiments at the Karlsruhe Research Accelerator (KARA), SOLEIL and MLS rings. Parameters of three simultaneous beams and alpha buckets at MLS and SOLEIL have been reproduced with high accuracy. General conditions for stable operation of alpha buckets are presented. Based on analytical formulas and computer simulations, studies of longitudinal motion at KARA have been performed with an objective to estimate feasibility of filling and storing of beam in α-buckets. A Computer model was used to describe the behavior and dynamics of simultaneous beams in the KARA storage ring.

Introduction

Short intense pulses of infrared Coherent Synchrotron Radiation (CSR) in the terahertz (THz) frequency range are generated at high energy electron storage rings and colliders when electron bunches are compressed to picosecond timescales [1]. These synchrotron radiation pulses generated by ultra-short electron bunches allow time-resolved x-ray experiments [2]. For this, special technics are applied to reduce the bunch length in electron storage rings. In the so-called "squeezed" operation mode, the high degree of spatial compression of the optics with reduced momentum compaction factor ("low-α optics") entails complex longitudinal dynamics of the electron bunches.

During experiments with low-α optics two and even three simultaneously rotating beams have been detected and observed at some light sources. A series of experiments have been conducted by a few synchrotron radiation facilities, namely: at Brookhaven National Synchrotron Light Source (NSLS) in the USA [3], SOLEIL in France [4], Metrological Light Source (MLS) in Germany [5,6], DIAMOND in the UK [7] where parameters of two, and even three beams, were measured and analyzed. By direct manipulation of nonlinear longitudinal beam dynamics a few beams were circulating in a ring with spatial separation and variable transverse sizes, positions, and energies depending on the RF frequency, sextupole and octupole (MLS) strengths. These beams are referred to as either 'RF' or 'α- bucket' beams, this depending on the RF phase that they occupy and energy; described later.

Dedicated studies of nonlinear momentum compaction factor and

associated beam parameters, as well as experiments with coherent synchrotron radiation, have been realized at MLS [8].

Dedicated operation with α-buckets is based on non-linear theory of longitudinal beam motion with high order terms of momentum compaction factor and requires control of compaction factor terms, precise adjustment of sextupole strength, high stability power supplies of all magnetic elements etc.

Linear and non-linear longitudinal beam dynamics in electron storage rings are well developed and presented in peer review journals [9], proceedings of CERN Accelerator Schools [10], proceeding of international accelerator conferences [11], manuscripts and books [12,13,14,15]. At low bunch current operation in high energy electron rings and when collective beam effects might be neglected, the so-called "zero current" bunch length is proportional to the square root of the ratio of momentum compaction factor α to the amplitude of RF voltage. The momentum compaction factor itself is a function of particle momentum offset from the reference orbit.

For systematic experimental observations of α-buckets, the longitudinal equations of motion should be expanded up to the third order terms of the momentum compaction factor. Thus, corresponding Hamiltonian equations describing longitudinal phase space should include fourth order terms of relative momentum deviation (δ4). For high energy offsets of more than a few percent, a higher order polynomial makes for a better fit to the orbit lengthening and momentum compaction factor as functions of energy offset.

Also, momentum independent Closed Orbit Deviation (COD) errors should be taken into account [4]. In general, path lengthening due to COD errors can be compensated by adjustment of RF frequency. But the dispersion function at low-α optics is highly stretched and then the beam orbit is captured by a dispersion pattern due to an energy shift generated by COD errors. Our experiments showed that compensation of coherent orbit oscillations is quite challenging for beam injection into negative and low-α optics [16].

In order to provide theoretical background for further studies and consistent explanation of the experiments with α-buckets we will cover some basics of longitudinal beam dynamics in Part 1 with emphasis on high order terms of orbit lengthening and momentum compaction factor. Based on Hamiltonian of longitudinal motion with fourth order terms in energy offset (δ^4), we will derive conditions for real solutions of the third order equation with a free independent term and analytical expressions for three real roots defining the energy gap between RF and α-buckets. Also, estimations of the free momentum independent relative orbit lengthening term (χ) will be provided as an example from the KArlsruhe Research Accelerator (KARA) ring. In Part 2 benchmarking analysis of existing experiments at SOLEIL [4] and MLS [5,6,8] rings will be performed based on analytical expressions derived in Part 1. The synchrotron frequency as a function of momentum offset and RF frequency deviation will be reproduced with high accuracy for both rings. Novel methods to estimate 'life-time' benchmarked on existing measurements at the MLS light source [5,8] will be proposed for discussion.

In Part 3 we will consider different options for α-buckets of the KARA storage ring including positive and negative momentum compaction factor optics. We will analyze and predict possible performance of future experiments with α-buckets and will estimate life-time at specific operation conditions.

Part 1. Theory of momentum compaction factor

Before proceeding to the analysis of low-α optics at different rings we would like to remind the reader basics and advanced features of beam longitudinal motion in electron storage rings. We will start from definitions and follow with the logics of standard theory expanded to high orders in momentum offset.

Orbit lengthening in electron storage rings

The Energy offset of a particle with respect to the reference particle energy E_0 written in units of momentum deviation is

$$\delta = \frac{p-p_0}{p_0} = \frac{\Delta p}{p_0} = \frac{1}{\beta_0}\frac{\Delta E}{E_0} \quad (1)$$

The Pass length element of a particle circulating in a ring and experiencing oscillations in horizontal and vertical directions (transverse planes are orthogonal to direction of motion) can be expressed in a Frenet-Serret coordinate system (s,x,z) (equation (9.94) of [12])

$$dl = \sqrt{\left(1+\frac{x}{\rho}\right)^2 (ds)^2 + (dx)^2 + (dz)^2} = ds\sqrt{\left(1+\frac{x}{\rho}\right)^2 + x'^2 + z'^2} \quad (2)$$

Here ds is the coordinates along the particular trajectory while dx and dz are deviations of particle trajectory from the reference orbit in horizontal and vertical planes respectively. Angular coordinates in phase space are defined as x′=dx/ds and z′=dz/ds. The term x/ρ in equation (2) represents a contribution to the pass length due to the curvature generated by bending magnets. The second (x′) and third (z′) terms are contributions due to finite horizontal and vertical betatron oscillations. The vertical bending magnets are omitted in equation (2) for simplicity.

The reference (equilibrium) orbit in a circular storage ring is defined as a closed trajectory in a median plane of a ring

$$r_{eo}(\theta + 2\pi) = r_{eo}(\theta) \equiv r_0 \quad (3a)$$

$$r'_{eo}(\theta + 2\pi) = r'_{eo}(\theta) \equiv r'_0 \quad (3b)$$

$$z(\theta + 2\pi) = z_{eo}(\theta) \equiv z_0 \quad (3c)$$

$$z'_{eo}(\theta + 2\pi) = z'_{eo}(\theta) \equiv z'_0 \quad (3d)$$

In the ideal case, the reference orbit is located in a median plane of a ring and deviations of the reference orbit in the vertical direction are absent (z_0=z'_0≡0). Furthermore, the deviations of the reference orbit in the horizontal direction (dispersion plane) are zeroed as well - (x_0=x'_0≡0).

Then, the length of a closed trajectory describing an equilibrium orbit for one turn might be found as an integral of trajectory of the reference particle

$$L_0 = \oint dl_{x=x'=z'=0} = \oint ds \quad (4)$$

In a storage ring, the orbit length L for off-momentum particles, as well as for particles deviating from the reference orbit, differs from the length of the reference orbit because of a few factors, for exam-

ple: dispersion in bending sections of a ring, betatron oscillations, uncorrelated closed orbit distortions (COD) leading to orbit deviations from trajectory of the synchronous particle. Now building on equation (4) the length of an arbitrary trajectory for one turn is the circular integral of pass length element dl is

$$L = \oint \left\{ \sqrt{\left(1 + \frac{x}{\rho}\right)^2 + x'^2 + z'^2} \right\} ds \tag{5}$$

For further consideration we should assume that for both vertical and horizontal oscillations all deviations from the reference orbit are small with respect to the radius of reference orbit and curvature radius of bending magnets ρ_0. Also that angular deviations are small

$$x = r - r_{eo} \ll \rho_0 \tag{6a}$$

$$x' \equiv \frac{\partial x}{\partial s} = r' - r'_{eo} \ll 1 \tag{6b}$$

$$z \ll \rho_0 \tag{6c}$$

$$z' \equiv \frac{\partial z}{\partial s} \ll 1 \tag{6d}$$

For small deviations one could apply an approximation

$$\sqrt{1+y} \approx 1 + \frac{y}{2} \tag{7}$$

Expanding the pass length variation $\Delta L = L - L_0$ over one turn up to second order deviations from the reference orbit x^2, x'^2, x^2, x'^2 gives

$$\Delta L = \oint \left\{ \sqrt{\left(1 + \frac{x}{\rho}\right)^2 + x'^2 + z'^2} \right\} ds - \oint ds \approx \oint \left(\frac{x}{\rho} + \frac{x^2}{2\rho^2} + \frac{x'^2}{2} + \frac{z'^2}{2} \right) ds \tag{8}$$

The length of a particle orbit depends on transverse coordinates and bending radius ρ. The particle oscillations in horizontal and vertical phase spaces are composed of betatron oscillations, residual closed orbit distortions (COD) and off-energy terms

$$x = x_\beta + x_{cod} + D\delta \tag{9a}$$
$$x' = x'_\beta + x'_{cod} + D'\delta \tag{9b}$$
$$z = z_\beta + z_{cod} \tag{9c}$$
$$z' = z'_\beta + z'_{cod} \tag{9d}$$

Here we consider a flat lattice with no dispersion in the vertical plane ($D_z = D'_z = 0$).

The amplitude of betatron oscillations can be derived from equation of beam envelope [12,13]

$$x_\beta = \sqrt{\beta_x \varepsilon_x} \qquad x'_\beta = \sqrt{\gamma_x \varepsilon_x} \qquad z_\beta = \sqrt{\beta_z \varepsilon_z} \qquad z'_\beta = \sqrt{\gamma_z \varepsilon_z} \tag{10}$$

High order terms of momentum compaction factor

In order to study non-linear beam dynamics in both longitudinal and transverse phase spaces one should consider variations of lattice parameters i.e. variation of dispersion function, Twiss parameters, momentum compaction factor etc. with respect to particle energy [17].

Chromatic dependence of the dispersion function expanded to the second order in momentum deviation δ can be written as [17].

$$D(s,\delta) = D_0(s) + D_1(s)\delta + D_2(s)\delta^2 + \ldots \tag{11}$$

Also, the derivative of dispersion along the orbit position (s) i.e. the slope of the dispersion function particle $D' \equiv \partial D/\partial s = 1/R$. $\partial D/\partial \theta$- can be expanded to the second order in momentum deviation δ

$$D'(s,\delta) \equiv \frac{\partial D}{\partial s} = D'_0(s) + D'_1(s)\delta + D'_2(s)\delta^2 + \ldots \tag{12}$$

Here $D_0(s)$, $D'_0(s)$ represent linear terms of the dispersion function and dispersion slope, and $D_1(s)$ $D'_1(s)$ of equation (13) represent the first derivative of the dispersion function in momentum as well as the first derivative of the dispersion function slope in momentum

$$D_1(s) = \frac{\partial D(s,\delta)}{\partial \delta} \qquad D'_1(s) = \frac{\partial D'(s,\delta)}{\partial \delta} \tag{13}$$

$D_2(s)$ $D'_2(s)$ in equation 14 is the second derivative of the dispersion function in momentum as well as second derivative in momentum of the dispersion function slope [17]

$$D_2(s) = \frac{1}{2}\frac{\partial^2 D(s,\delta)}{\partial \delta^2} \qquad D'_2(s) = \frac{1}{2}\frac{\partial^2 D'(s,\delta)}{\partial \delta^2} \tag{14}$$

High order terms of dispersion function (13) and its slope (14) should be included into the chromatic part of equation for particle oscillations (9). Now one can write expressions of particle oscillations expanded to the third order of momentum deviation δ

$$x = x_\beta + x_{cod} + D_0(s)\delta + D_1(s)\delta^2 + D_2(s)\delta^3 \tag{15a}$$
$$x' = x'_\beta + x'_{cod} + D'_0(s)\delta + D'_1(s)\delta^2 + D'_2(s)\delta^3 \tag{15b}$$
$$z = z_\beta + z_{cod} \tag{15c}$$
$$z' = z'_\beta + z'_{cod} \tag{15d}$$

Substituting equations of particle oscillations (15) into the equation for pass length variation (8) and evaluating the integral one can derive an equation of orbit lengthening due to chromatic as well as amplitude dependent orbit oscillations.

It should be noted that linear terms in the expression for orbit lengthening (8) after averaging over many turns consequently vanish due to oscillatory behavior of betatron motion [12]

$$\langle x_\beta \rangle = \langle z_\beta \rangle = \langle x'_\beta \rangle = \langle z'_\beta \rangle = 0 \tag{16}$$

The linear part of orbit distortions is statistical in nature, therefore, orbit correction in accelerators is done so as to minimize residual COD errors

$$\langle x_{cod} \rangle = \langle z_{cod} \rangle \approx 0 \tag{17}$$

Betatron oscillations and CODs are completely independent and therefore all cross terms like $\langle x\beta x cod \rangle$ are vanished

$$\langle x_\beta x_{cod} \rangle = \langle x'_\beta x'_{cod} \rangle = \langle z'_\beta z'_{cod} \rangle = 0 \tag{18}$$

As stable operation of a storage ring is achieved at non-resonance tunes $Q_x \neq k$, $Qz \neq l$ (not integer), then cross terms like $\langle x\beta D O\delta \rangle$ are vanished as well

$$\langle x_\beta (D_0\delta) \rangle = \langle x_{cod} (D_0\delta) \rangle = \langle x'_\beta (D'_0\delta) \rangle = \langle x'_{cod} (D'_0\delta) \rangle = 0 \tag{19}$$

With these assumptions, the pass length variation defined by equation (8) can be split into two parts; one independent on momentum deviation (details of this contribution will be analyzed later) and the other dependent on high order terms of momentum offset δ

$$\Delta L = \frac{1}{2}\oint\left(x'^2_\beta + z'^2_\beta + x'^2_{cod} + z'^2_{cod} + \frac{x^2_\beta}{\rho^2} + \frac{x^2_{cod}}{\rho^2}\right)ds \quad (20a)$$

$$+\left[\oint\left(\frac{D_0}{\rho}ds\right)\right]\delta \quad (20b)$$

$$+\left[\oint\left(\frac{D_0^2}{2\rho^2} + \frac{D_1}{\rho} + \frac{D'^2_0}{2}\right)ds\right]\delta^2 \quad (20c)$$

$$+\left[\oint\left(\frac{D_0 D_1}{2\rho^2} + \frac{D_2}{2\rho} + D'_0 D'_1\right)ds\right]\delta^3 \quad (20d)$$

The basic equation for orbit lengthening truncated to the second order in energy deviation δ^2 is presented in [12]. One can also find a high order equation of orbit lengthening truncated to the third power of momentum offset δ^3, but with slightly different definitions in [4].

The momentum compaction factor αp is defined as the relative change of orbit length with respect to momentum deviation. Thus, the chromatic part of relative orbit lengthening (20b,c,d) might be expressed as [13,18].

$$\left(\frac{\Delta L}{L_0}\right)_{chr} = \alpha(\delta)\cdot\delta \quad (21)$$

Momentum compaction factor itself depends on energy offset and is, up to the second order of energy deviation δ, defined as [4,12]

$$\alpha(\delta)=\alpha_1+\alpha_2\delta+\alpha_3\delta^2 \quad (22)$$

Linear and high order components of the momentum compaction factor are derived from equations (20,21,22) and can be written as

$$\alpha_1 = \frac{1}{L_0}\oint\left(\frac{D_0}{\rho}ds\right) \quad (23)$$

$$\alpha_2 = \frac{1}{L_0}\left[\oint\left(\frac{D_0^2}{2\rho^2} + \frac{D_1}{\rho} + \frac{D'^2_0}{2}\right)ds\right] \quad (24)$$

$$\alpha_3 = \frac{1}{L_0}\left[\oint\left(\frac{D_0 D_1}{\rho^2} + \frac{D_2}{2\rho} + D'_0 D'_1\right)ds\right] \quad (25)$$

where the first term of momentum compaction factor, α1, is an integral of linear dispersion $D_0(s)$ inside the dipoles of bending radius ρ. The linear term of dispersion is often better written as function of longitudinal orbit position (s) [13,17]

$$D_0(s_0) = \frac{\sqrt{\beta_{x(s_0)}}}{2sin(\pi Q_x)}\oint\frac{\sqrt{\beta_{x(s)}}}{\rho(s)}cos[\pi Q_x - |\mu_x(s)-\mu_x(s_0)|]ds \quad (26)$$

The second term of the dispersion function (equation (11), is the first derivative of dispersion in momentum offset D1(s)=∂D(s,δ)/∂δ. It is proportional to the product of sextupole strength ($K_{SXT}=1/B0\rho 0.\partial^2 B/\partial R^2$) and the third power of linear dispersion $D_0^3(S)$ [19], and can be written as

$$D_1(s_0) = -D_0(s_0) + \frac{\sqrt{\beta_{x(s_0)}}}{2sin\pi Q_x}\oint\left\{\left[K_0(s) - K_{SXT}(s)D_0(s)\right]\times D_0(s)\sqrt{\beta_x(s)}\,cos[\pi Q_x - |\mu_x(s-s_0)|]\right\}ds \quad (27)$$

This is very useful as the value, and even the sign, of the second term of compaction factor α_2 can be modified by variation of the second order term of Dispersion D_1, see equation (24). For example, a dedicated family of chromatic sextupoles could therefore control the quadratic term of momentum compaction factor [20]

$$\Delta\alpha_2 = -\frac{1}{2L_0}\oint\frac{\Delta D_1(s)}{\rho(s)}ds = -\frac{1}{2L_0}\oint D_0^3\cdot\Delta K_{SXT}ds \quad (28)$$

Equations of motion in longitudinal phase space including high order terms of momentum deviation

In this section we analyze equations of synchrotron oscillations in longitudinal phase space while including high order terms in momentum deviation. Summarizing equations (20) to (25) the pass length variation is split into a chromatic part dependent on high order momentum compaction factor and another part independent on momentum deviation. The chromatic part of relative orbit lengthening $(\Delta L/L_0)_{chr}$ is described by high order terms of compaction factor and expressed by equations (21) and (22).

The momentum independent term of relative orbit lengthening (χ) includes betatron oscillations and COD errors, see equation (20a), and is now given as

$$\chi \equiv \left(\frac{\Delta L}{L_0}\right)_{\beta,COD} = \frac{1}{2L_0}\oint\left(x'^2_\beta + z'^2_\beta + x'^2_{cod} + z'^2_{cod} + \frac{x^2_\beta}{\rho^2} + \frac{x^2_{cod}}{\rho^2}\right)ds \quad (29)$$

The contribution of each element into the momentum independent orbit length variation, and the evaluation case of the KARA storage ring will be discussed later.

The relative orbit lengthening is composed of chromatic part and free momentum independent orbit lengthening term χ, and can be written, up to the third order in energy deviation, in a following form [4]

$$\frac{\Delta L}{L_0} = \left(\frac{\Delta L}{L_0}\right)_{chr} + \chi = \alpha_3\delta^3 + \alpha_2\delta^2 + \alpha_1\delta + \chi \quad (30)$$

The complete equation of relative orbit lengthening, equation (30), is similar to the second order equation from [21] as well as to the second order equation (6.3) from [12] but expanded up to the higher order in momentum offset.

To derive conditions for the longitudinal phase space stability under influence of high order terms of momentum compaction factor, one should also evaluate the Hamiltonian using high order momentum deviation [3,20,21].

Energy balance in an electron storage ring is defined as when the energy losses caused by synchrotron radiation W_{SR} are compensated by the energy gained by RF voltage

$$eU_{RF}\cdot sin\varphi \geq W_{SR}(E) \quad (31)$$

In electron storage rings the synchronous phase (φs) is determined as when the energy gain, supplied by RF, is equal to energy loss due to synchrotron radiation

$$sin\varphi_s = \frac{W_{SR}(E_s)}{eU_{RF}} \quad (31a)$$

Also, beam energy loss per turn, due to synchrotron radiation, can be estimated in practical units [14]

$$\frac{W_{SR}(E)}{turn} \approx 88.5\frac{E_0^4[GeV]}{\rho[m]} \quad (32)$$

where E_0 is the energy of the synchronous particle and ρ is the radius of bending magnets. The synchronous particle is represented in longitudinal phase space by synchronous energy (E_0) and synchronous phase φ_S). Particles of non-synchronous phase (φ) or non-synchronous energy (E) experience oscillations in phase and energy around the synchronous particle. The energy change per turn can be described by

$$\frac{\Delta E}{turn} = eU_{RF} \cdot sin\varphi - \frac{W_{SR}(E_0)}{turn} \quad (33)$$

As synchrotron oscillations are slow in comparison to the rotation period of particle (T_0), the energy change per turn could be substituted by the derivative

$$\frac{\Delta E}{turn} \approx \frac{dE}{dn} \quad (34)$$

Furthermore, as the pass length per turn is a product of electron speed and rotation period

$$\frac{ds}{dn} = \beta_0 c T_0 \quad (35)$$

Now substituting variables $dE/dn=(dE/ds)\cdot(ds/dn)$ and transferring to momentum deviation (δ) instead of energy change (ΔE)

$$\frac{d\delta}{ds} = \frac{1}{\beta_0^2 E_0}\frac{d(\Delta E)}{ds} \quad (36)$$

one comes to first equation of synchrotron oscillations [12,13,21]

$$\frac{d\delta}{ds} = \frac{F_0}{\beta_0^3 c}\frac{eU_{RF}}{E_0}[sin\varphi - sin\varphi_s] \quad (37)$$

where F_0 is rotation frequency of particle.

The second equation of synchrotron oscillations is derived from RF phase relations. Decrement of particle RF phase can be expressed via the ring azimuth change

$$\Delta\varphi = \varphi - \varphi_s = h_{rf}\Delta\theta \quad (38)$$

The relation between azimuth and rotation period is $\Delta\theta = 2\pi\Delta T/T_0$. The relation between rotation period and orbit length is $T_0 = L_0/\beta_{0C}$. And the relation between change of rotation period and change of orbit length is $\Delta T = \Delta L\beta c$. All three relationships are substituted in to the expression for RF phase shift (38). Variation of RF phase per turn can also be accounted for as it is directly proportional to relative change of orbit length $\Delta L/L_0$ i.e. to the first and high order terms of momentum compaction factor, see equation (30) [4,21]

$$\frac{\Delta\varphi}{turn} = 2\pi h_{rf}\left(\frac{\Delta L}{L_0}\right) \quad (39)$$

As stated earlier, synchrotron oscillations are slow in comparison to the rotation period of particle (T_0) and the change of RF phase per turn could be approximated, similar to energy change, by derivative $\Delta\varphi/turn \approx d(\Delta\varphi)/dn$, see equation (34).

Substituting variables $d(\Delta\varphi)/dn=(d(\Delta\varphi)/ds)\cdot(ds/dn)$ and using equation (35) for pass length, one derives the second equation of synchrotron oscillations which includes high order terms of compaction factor and a free term defined by momentum independent orbit errors

$$\frac{d(\Delta\varphi)}{ds} = \frac{2\pi h_{rf}}{\beta_0 c}F_0\left(\frac{\Delta L}{L_0}\right) \quad (40)$$

where h_{rf} is RF harmonic and $F_{rf}=h_{rf}F_0$ is the frequency of RF cavity.

From the two differential equations, i.e. first order for momentum deviation (37) and RF phase deviation (40), we can get one second order equation of synchrotron oscillation. Again, substituting length variable (s) by the time variable (t),

$$\frac{d^2}{ds^2} = \frac{1}{(\beta_0 c)^2}\frac{d^2}{dt^2} \quad (41)$$

one can derive the second order differential equation for small momentum deviations [12]

$$\frac{d^2\delta}{dt^2} + F_s^2\delta = 0 \quad (42)$$

Similar equation can be written for phase oscillations. The synchrotron tune, F_s, depends on high order terms of the momentum compaction factor [4], where α can be defined as a derivative of the relative orbit lengthening with momentum offset $\alpha = \partial(\Delta L/L_0)/\partial\delta$ [18, 21], see equation (21)

$$F_s(\delta) = F_0\sqrt{\frac{h_{rf}eU_{rf}(-cos\varphi_s)}{2\pi\beta_0^2 E_0}}\cdot\sqrt{(\alpha_1 + 2\alpha_2\delta + 3\alpha_3\delta^2)} \quad (43)$$

At positive values of momentum compaction factor, ($\alpha_1>0$), oscillations of particles in longitudinal phase space (Δ_φ,δ), are stable for negative slopes of the RF voltage sinusoidal wave $U=U_{RF}\cdot Sin(\omega t)$, i.e. at RF phases ($\pi/2<\varphi_s<\pi$). The minus sign "-" was included in equation (43) for synchrotron frequency in order to get a real value of synchrotron tune for a Stable Fixed Point (SFP) when the compaction factor is positive ($\alpha_1>0$) while ($\cos\varphi_s<0$).

At negative slopes of the RF voltage curve, particles with an energy higher than the reference one, $E>E_0$ (positive momentum offset $\delta>0$), travel a longer way with respect to the reference particle ($\Delta L>0$) and will be delayed. Next turn electrons with initially higher energy will gain less energy than equilibrium particles and the difference in energy will be reduced.

Synchrotron oscillations are stable and the same stability criteria is applied for particles with different RF phases $\Delta\varphi$. For a negative linear compaction factor ($\alpha_1<0$), oscillations are stable for positive slopes of the RF voltage curve ($0<\varphi<\pi/2$) and stable phase is ($\pi-\varphi s$). Unstable Fixed Points (UFP) with crossed branches of separatrix are located at phase (φs) for negative compaction factor ($\alpha 1<0$), and at phase ($\pi-\varphi s$) for a positive linear term ($\alpha 1>0$).

Hamiltonian of motion in longitudinal phase space

One can rewrite synchrotron equations (37) and (40), by substituting the length variable (s) by the time variable (t) using the relation $d/ds=1/\beta c\cdot d/dt$

$$\frac{d\delta}{dt} = \frac{F_0}{\beta_0^2}\frac{eU_{RF}}{E_0}[sin(\varphi_s + \Delta\varphi) - sin\varphi_s] \quad (37a)$$

$$\frac{d(\Delta\varphi)}{dt} = 2\pi h_{rf}F_0(\alpha_3\delta^3 + \alpha_2\delta^2 + \alpha_1\delta + \chi) \quad (40a)$$

The Hamiltonian operator, describing longitudinal phase space [12,18,20], can be constructed using deviation of RF phase ($\Delta\varphi$) and momentum offset (δ) as canonical conjugate variables, and applying canonical equations

$$\frac{\partial H}{\partial \delta} = \frac{d(\Delta\varphi)}{dt} \quad (44a) \qquad \frac{\partial H}{\partial (\Delta\varphi)} = -\frac{d\delta}{dt} \quad (44b)$$

The Hamiltonian function of a particle motion in longitudinal phase space is an integral of canonical equations (41a, b)

$$H = \int \frac{d(\Delta\varphi)}{dt}\, d\delta - \int \frac{d\delta}{dt}\, d(\Delta\varphi) \quad (45)$$

Substituting synchrotron equations (37a) and (40a) into the integral expression of Hamiltonian equation (45), one can derive a full Hamiltonian operator of longitudinal motion, including high order terms of momentum compaction factor [4,20]

$$H = 2\pi h_{rf} F_0 \left(\frac{1}{4}\alpha_3\delta^4 + \frac{1}{3}\alpha_2\delta^3 + \frac{1}{2}\alpha_1\delta^2 + \chi\delta\right) + \frac{F_0}{\beta_0^2}\frac{eU_{RF}}{E_0}\left[cos(\varphi_s + \Delta\varphi) - cos(\varphi_s) + \Delta\varphi \cdot sin(\varphi_s)\right] \quad (46)$$

The Hamiltonian is a constant of motion in time. Locations of fixed points, where canonical conjugate variables are constant in time, can be derived from two conditions:

$$\frac{\partial H}{\partial \delta} = \frac{d(\Delta\varphi)}{dt} = 0 \quad (47a) \qquad \frac{\partial H}{\partial (\Delta\varphi)} = -\frac{d\delta}{dt} = 0 \quad (47b)$$

Condition of fixed momentum offset, equation (47b), is realized if $Sin(\varphi s+\Delta\varphi) - Sin\ \varphi s = 0$. This equation has two solutions for RF phase of fixed points

$$\varphi = \varphi_s \quad (48a) \qquad \varphi = \pi - \varphi_s \quad (48b)$$

Condition of fixed phase, equation (47a), is fulfilled when the relative orbit lengthening is zeroed

$$\alpha_3\delta^3 + \alpha 2\delta^2 + \alpha_1\delta + \chi = 0 \quad (49)$$

Solutions of longitudinal equations of motion with high order terms of momentum compaction factor

In this section we consider solutions of longitudinal equations of motion up to the third order terms of the momentum compaction factor. Equation (49) is a third order general cubic equation with a free momentum independent term χ. Usually it is solved by Cardano method [22]. Original attempts to find solutions to a Cardano equation led to the introduction of complex variables [23]. Cubic equation (49) has always three roots. At least one of these roots is real, while the other roots are complex [24]. With some conditions all three roots of cubic equation are real. Real roots represent focus points inside of stable buckets and are referred to as Stable Fixed Points (SFP) [25]. Complex roots represent unstable motion - saddle points where two separatrixes are crossed – Unstable Fixed Points (UFP) [25].

Approximation of negligible momentum independent term

Neglecting (at this moment only) the energy independent term (χ=0), one can simplify and split equation (49) into two parts. The first part has one root corresponding to on-momentum synchronous particles (δ_1=0). For a positive momentum compaction factor (α>0) the phase of a synchronous particle is (φ_s). The area of stable oscillations in longitudinal phase space around a synchronous particle is referred to as an RF bucket [8,10,20]. The second part is a quadratic equation

$$\alpha_3\delta^2 + \alpha_2\delta + \alpha_1 = 0 \quad (50)$$

Solutions of second order equation (50) provide another two roots with momentum offset

$$\delta_{2,3} = \frac{1}{2\alpha_3}\left[-\alpha_2 \pm \sqrt{\alpha_2^2 - 4\alpha_1\alpha_3}\right] \quad (51)$$

Conditions of stable motion around off-momentum focal points are defined by high order components of momentum compaction factor. Roots of the reduced second order equation (51) should be real in order to satisfy the stability criteria; namely:

- if the first and third order terms of compaction factor are of the same sign, then the absolute value of second term should be larger than double the square root of their product

$$|a_2| > 2\sqrt{\alpha_1\alpha_3} \quad (52)$$

- if $|a_2| < 2\sqrt{\alpha_1\alpha_3}$ then the first α_1, and third α_3 order terms of momentum compaction factor should be of different sign. For $\alpha_1 > 0$ the $\alpha_3 < 0$ and vice versa.

The area of stable motion in longitudinal phase space around SFPs with momentum offset δ_2 or δ_3 is referred as alpha-bucket (α-bucket) [8,20,21]. α-buckets are shifted in energy and in RF phase (in time) from RF buckets (see earlier for RF buckets). For a positive compaction factor ($\alpha 1 > 0$), RF buckets are located at phase (φ_s) while α-buckets – at phase ($\pi - \varphi_s$).

When the first α_1, and third α_3 order terms of momentum compaction factor are of same sign and absolute value of second term $|a2| < 2\sqrt{\alpha_1\alpha_3}$, then one real (stable) solution exists. Roots $\delta_{2,3}$ of the second order equation (50) are complex and RF motion around these fixed points is unstable

$$\delta_{2,3} = \sqrt{\frac{\alpha_1}{\alpha_3}}\, exp\left\{\left[\pm arct\left(\sqrt{\frac{4\alpha_1\alpha_3}{\alpha_2^2} - 1}\right)\right] i\right\} \quad (53)$$

General solution of third order equation with free momentum independent term

One should acknowledge that in the general case when free term (χ) is not negligible, there is no solution with reference energy i.e. with zero momentum offset (δ=0). All roots of the cubic equation are shifted in momentum from the reference orbit if COD errors are not compensated for ($\chi \neq 0$).

The solution of the cubic equation involves a "discriminant" whose sign determines the number of real solutions, as with the quadratic equation. But more complicated techniques should be applied [26]. Three roots of the cubic equation (49) require finding the cube roots with either real or complex numbers

$$\delta_1 = -\frac{a_2}{3a_3} + \frac{1}{\sqrt[3]{2}(3a_3)}\left\{\sqrt[3]{-\Delta_1 + \sqrt{-\Delta}} + \sqrt[3]{-\Delta_1 - \sqrt{-\Delta}}\right\} \quad (54)$$

$$\delta_2 = -\frac{a_2}{3a_3} - \frac{1}{2\sqrt[3]{2}(3a_3)}\left\{\sqrt[3]{-\Delta_1 + \sqrt{-\Delta}} + \sqrt[3]{-\Delta_1 - \sqrt{-\Delta}} - i\sqrt{3}\left[\sqrt[3]{-\Delta_1 + \sqrt{-\Delta}} - \sqrt[3]{-\Delta_1 - \sqrt{-\Delta}}\right]\right\} \quad (55)$$

$$\delta_3 = -\frac{a_2}{3a_3} - \frac{1}{2\sqrt[3]{2}(3a_3)}\left\{\sqrt[3]{-\Delta_1 + \sqrt{-\Delta}} + \sqrt[3]{-\Delta_1 - \sqrt{-\Delta}} + i\sqrt{3}\left[\sqrt[3]{-\Delta_1 + \sqrt{-\Delta}} - \sqrt[3]{-\Delta_1 - \sqrt{-\Delta}}\right]\right\} \quad (56)$$

In equations (54), (55) and (56) the third order determinant Δ1 includes the momentum independent free term χ

$$\Delta 1 = 2a_2^3 - 9a_1a_2a_3 + 27a_3^2\,\chi \quad (57)$$

The second order determinant (−Δ0) is described by the equation

$$(-\Delta_0) = 3a_1a_3 - a_2^2 \quad (58)$$

The general determinant (−Δ) is a composition of third and second order determinants [17]

$$(-\Delta) = \Delta_1^2 + 4(-\Delta 0)^3 \quad (59)$$

and is related to the classical determinant Q of reduced cubic Cardano equation [10] as

$$(-\Delta) = Q\cdot[4\cdot(3a_3)^6] \quad (60)$$

- If the general determinant of the cubic equation (49) is negative, (−Δ)<0 (Q<0), then all three roots $\delta_1,\delta_2,\delta_3$ are real
- If the determinant of the cubic equation is positive (−Δ)>0 (Q>0) then one root is real, see equation (54) and two other roots are complex, see equations (55) and (56)
- If the determinant of the cubic equation is equal to zero, (−Δ)=0 (Q=0) ,then two real roots exist: first root is δ1 and second root is $\delta_2=\delta_3$

The minus sign for the second order discriminant, $(-\Delta_0)$, as well as for discriminant, (−Δ), were introduced here in order to be consistent with the definition of the classical determinant Q [17]. In an approximation of the negligible momentum independent term (χ=0), the square root of determinant (−Δ) is simplified to

$$\sqrt{(-\Delta)_{\chi=0}} = 3\sqrt{3}\,a_1a_3\sqrt{4a_1a_3 - a_2^2} \quad (61)$$

For (χ=0) and ($a_2^2>4a_1a_3$) the square root of determinant √(−Δ) χ=0 is a complex number leading to one root of equation (55) to be equal to zero ($\delta_2=0$), while two other roots (δ_1,δ_3) of equations (54) and (56) are real numbers equal to solutions (51) of quadratic equation (50). According to Vieta's formulas [28], roots of the cubic equation with a free term, equation (49), are related to each other as

$$\delta_1 + \delta_2 + \delta_3 = -\frac{a_2}{a_3} \quad \text{and} \quad \frac{1}{\delta_1} + \frac{1}{\delta_2} + \frac{1}{\delta_3} = -\frac{a_1}{\chi} \quad (62a)$$

$$\delta_1\delta_2 + \delta_2\delta_3 + \delta_1\delta_3 = \frac{a_1}{a_3} \quad \text{and} \quad \frac{1}{\delta_1\delta_2} + \frac{1}{\delta_2\delta_3} + \frac{1}{\delta_1\delta_3} = \frac{a_2}{\chi} \quad (62b)$$

$$\delta_1\cdot\delta_2\cdot\delta_3 = -\frac{\chi}{a_3} \quad \text{and} \quad \frac{1}{\delta_1\cdot\delta_2\cdot\delta_3} = -\frac{a_3}{\chi} \quad (62c)$$

If the free term of the cubic equation is equal to zero (in our case the momentum independent term (χ=0)) then at least one of the roots of general equation (49) is equal to zero. We are interested in a case where all three roots $\delta_1,\delta_2,\delta_3$ are REAL values, i.e. determinant of cubic equation is negative (−Δ)<0 and the square root of determinant (√(−Δ)) is a complex number. Three real roots might be found according to the following equations

$$\delta_1 = -\frac{a_2}{3a_3} + \frac{2}{\sqrt[3]{2}(3a_3)}\left\{\sqrt[3]{\sqrt{\Delta_1^2 + |-\Delta|}}\cos\left(\frac{\varphi}{3}\right)\right\} \quad (63)$$

$$\delta_2 = -\frac{a_2}{3a_3} - \frac{1}{\sqrt[3]{2}(3a_3)}\left\{\sqrt[3]{\sqrt{\Delta_1^2 + |-\Delta|}}\left[\cos\left(\frac{\varphi}{3}\right) + \sqrt{3}\sin\left(\frac{\varphi}{3}\right)\right]\right\} \quad (64)$$

$$\delta_3 = -\frac{a_2}{3a_3} - \frac{1}{\sqrt[3]{2}(3a_3)}\left\{\sqrt[3]{\sqrt{\Delta_1^2 + |-\Delta|}}\left[\cos\left(\frac{\varphi}{3}\right) - \sqrt{3}\sin\left(\frac{\varphi}{3}\right)\right]\right\} \quad (65)$$

Tangent of angle φ is defined in equations (63) to (65) as the ratio

$$tg(\varphi) = \frac{\sqrt{|-\Delta|}}{(-\Delta_1)} \quad (66)$$

where the angle φ is the main argument between $-\pi/2<\varphi<+\pi/2$. One should take care of the sign of the $Sin(\varphi)$ function when angle φ is negative.

KARA storage ring lattice at different operation modes

Simulations of orbit lengthening due to COD errors and betatron motion were performed on example of the KARA lattice [29]. The optics of the KARA storage ring is tuned during 'user operation' to double bend achromat (DBA) conditions with $D=D'=0$ in straight sections, and to a Theoretical Minimum Emittance (TME) condition where dispersion D, and horizontal betatron function βx, are minimized at the location of the bending magnets [29]. For TME mode, the dispersion function is always positive and varies from +0.11 to +0.74 m. Dispersion does leak in to straight section and is equal to +0.35 m for both long and short straight sections (Figure 1) [30].

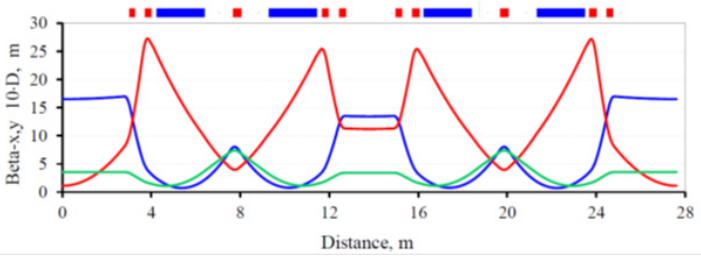

Figure 1: One cell of the KARA lattice is composed of two pairs of 22.50 bends. The TME operation mode with distributed dispersion function is shown. The horizontal/vertical beta-functions are plotted in blue/red respectively, and dispersion (is zoomed in 10 times [29,30].

In order to reduce the compaction factor to a low value, or make it negative ($\alpha_1<0$), one should compensate positive contribution of the linear dispersion function inside bending magnets by negative dispersion. One can minimize the momentum compaction factor (squeeze α) as well as reverse the sign of α to a negative one by varying the strength of the Q3 family of quads, see Figure 2 [31]. For example, by increasing the strength of the Q3 quads, it is possible to stretch the dispersion function from +1.44 m in the middle

of the bending section (approx. at Q3) to -1.03 m in all straight sections, thus reducing compaction factor from α_1=+9.10^{-3} to α_1=+1.10-4 as shown in Figure 2. By a small additional increase of Q3 strength the dispersion is further stretched from a highly positive value +1.5m to a negative one -1.1 m and the momentum compaction factor is reversed to a negative value, α_1=-2.10−3[31].

In order to compensate shift of radial Q_x and vertical Q_z betatron tunes during the squeezing procedure, the strength of other quadrupoles is adjusted as well.

In particular, for positive low -α operation mode the strengths of Q1, Q2, Q4 and Q5 quadrupole families are monotonically reduced while strength of Q3 family is gradually increased. A similar procedure, but in reverse order, is applied for the negative compaction factor to approach low-α optics.

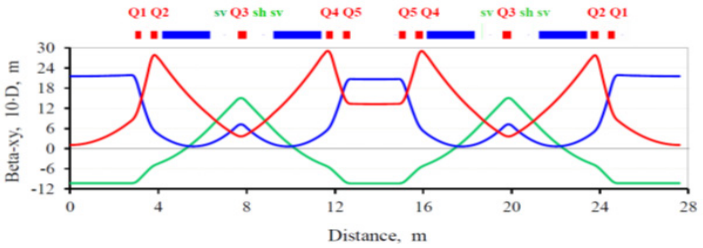

Figure 2: One cell of KARA storage ring lattice at low positive compaction factor α=+1.10-4. Dispersion function is stretched from +1.44 m down to -1.03 m in order for negative contribution to compensate positive one inside bending magnets. **Blue** curve is horizontal beta function βx, **red** -vertical function βy, **green** -zoomed in 10 times dispersion *D0* [31].

Longitudinal-transverse beam coupling and estimation of momentum independent term χ

The momentum independent term of relative orbit lengthening (χ) includes betatron oscillations and CODs and it is described by equation (29). We would like to now consider the contribution of the momentum independent free term into orbit lengthening on example of the KARA storage ring.

Contribution of betatron motion into orbit lengthening

The contribution of betatron oscillation terms in equation (29) might be further simplified by using Twiss parameters and explicit expressions for particle motion [32]

$$x_\beta(s) = \sqrt{\beta_x(s)\varepsilon_x}\,\sin\mu_x(s) \tag{67a}$$

$$x'_\beta(s) = \sqrt{\varepsilon_x/\beta_x(s)}\,[\cos\mu_x(s) - \alpha_x(s)\sin\mu_x(s)] \tag{67b}$$

The finite value of emittance, ε_x, is used here as the amplitude factor for the betatron oscillation and therefore, provides orbit length spread within the beam cross section. One can estimate the contribution of quadratic angular deviation of a beam into orbit lengthening by substituting equation (67b) into equation (29)

$$\frac{1}{2L_0}\oint\left(x'^2_\beta\right)ds = \frac{\varepsilon_x}{2L_0}\oint\frac{1}{\beta_x}[\cos^2\mu_x - 2\alpha_x\cos\mu_x\sin\mu_x + \alpha_x^2\sin^2\mu_x]ds =$$

$$= \frac{\varepsilon_x}{2L_0}[\oint\gamma_x ds]\left[\oint_0^L(\sin^2\mu_x)ds\right] = \frac{1}{4}\varepsilon_x\langle\gamma_x\rangle \tag{68}$$

Here $\langle\gamma x\rangle$ is an average value of Twiss parameter γ_x in a ring. A similar expression can be derived for vertical components of average quadratic angle $12L_0/\int(z'\beta^2)\,ds$=1/4 εz$\langle\gamma_z\rangle$. One can neglect any contribution of vertical quadratic angle in a flat lattice ring with horizontal bending, when vertical emittance is much less than the horizontal one $\varepsilon_z \ll \varepsilon_x$.

Contribution of the quadratic term of horizontal betatron motion inside bending magnets can be estimated by substituting equation (67a) into equation (29). Integration should be performed at the a*zimuthal position of bending magnets*

$$\frac{1}{2L_0}\oint\left(\frac{x_\beta^2}{\rho^2}\right)ds \cong \frac{\varepsilon_x}{4}\left[\oint_0^{2\pi}\left(\frac{\beta_x}{\rho^2}\right)d\theta\right] = \frac{\pi}{2}\frac{\langle\beta_x\rangle_b}{\rho^2}\varepsilon_x \tag{69}$$

where βx_b is an average value of horizontal betatron function at the azimuth of bending magnets.

We use the following parameters in order to estimate a contribution of betatron motion in the orbit lengthening of KARA storage ring

- Radius of bending magnets ρ=5.56 *m*
- Average Twiss parameter gamma $\langle\gamma_x\rangle$=0.4 m^{-1}
- Average value of betatron function in bending magnets is slightly changed from

$\langle\beta_x\rangle_b$=1.8 *m* for 'user operation' mode (momentum compaction factor α=9.10-3 to

$\langle\beta_x\rangle_b$=2.0 *m* for negative compaction factor operational mode (α=-7.10-3)

In total, the momentum independent contribution of betatron motion could be estimated for KARA storage ring by following expression

$$\left(\frac{\Delta L}{L_0}\right)_\beta = \frac{1}{2L_0}\oint\left(x'^2_\beta + \frac{x_\beta^2}{\rho^2}\right)ds \cong 0.23\varepsilon_x \tag{70}$$

Equation (70) is dimensionless, as the value of emittance is provided in [*m*]. Orbit lengthening due to betatron motion is directly proportional to beam emittance and naturally grows with increasing beam energy since emittance is proportional to $\epsilon_x \sim\gamma^2$.

According to [12], one should include the tails of a Gaussian distribution of an electron beam,and use the value of emittance εx-≈7εx^{rms}, for accurate estimation of betatron contribution to orbit lengthening. Nevertheless, in order to be consistent, we use the "rms" values of beam parameters at equilibrium after synchrotron damping. The contribution of betatron motion to relative orbit lengthening at different energies and operation modes of the KARA storage ring is shown in Table 1, where values in blue outline growth of emittance and orbit lengthening due to Intra-Beam Scattering (IBS) for 2 mA/bunch beam.

Table 1: Contribution of betatron motion to relative orbit lengthening for the KARA storage ring at different energies and operation modes. Values in blue outline contributions of IBS to the beam emittance growth for 2 mA/bunch beam.

Modes/momentum compaction factor	TME mode $\alpha 1 = +9.10^{-3}$	Low-α $\alpha 1 = +1.10^{-4}$	Low neg.-α $\alpha 1 = -1.10^{-4}$	Negative-α $\alpha 1 = -2.10^{-3}$	High neg. α $\alpha 1 = -9.10^{-3}$
Beam energy	0.5 GeV				
$\varepsilon_x^{rms}(\epsilon_x + IBS)$	2.4 (24)	12 (36)	12 (36)	13 (40)	20 (45)
$(\Delta L/L_0)\beta$ $+IBS$	6.10^{-10} (6.10^{-9})	$2.8.10^{-9}$ $(8.4.10^{-9})$	$2.8.10^{-9}$ $(8.4.10^{-9})$	3.10^{-9} (9.10^{-9})	5.10^{-9} $(1.2.10^{-8})$
Beam energy	1.3 GeV				
ε_x^{rms} (nm)	16	80	80	90	140
$(\Delta L/L0)_\beta$	4.10^{-9}	$1.8.10^{-8}$	$1.8.10^{-8}$	$2.1.10^{-8}$	$3.2.10^{-8}$
Beam energy	2.5 GeV				
ε_x^{rms} (nm)	60	300	300	340	500
$(\Delta L/L_0)_\beta$	$1.4.10^{-8}$	7.10^{-8}	7.10^{-8}	8.10^{-8}	$1.2.10^{-7}$

For estimation purposes we convert emittance values to the beam size, σβ (rms), at the middle of the long straight section of the KARA storage ring where horizontal betatron function is β_x=17 m for user TME mode and β_x=20 m at low-α mode, see Table 2.

Table 2: Converting emittance to beam size σβ (rms) in the middle of long straight section of KARA storage ring. β_x=20 m at low-α and β_x=17 m at user TME modes.

ε_x (nm) $+IBS$	2.4 24	12 36	13 40	16 42	20 45	80	140	300	340	500
σβ, mm	0.2 0.7	0.49 0,85	0.51 0.9	0.56 0.91	0.63 1	1.26	1.67	2.45	2.6	3.16
$(\Delta L/L_0)_\beta$	6.10^{-10} 6.10^{-9}	$2.8.10^{-9}$ 9.10^{-9}	3.10^{-9} 10-8	4.10^{-9} 10^{-8}	5.10^{-9} $1.2.10^{-8}$	2.10^{-8}	3.10^{-8}	7.10^{-8}	8.10^{-8}	$1.2.10^{-7}$

Relative orbit lengthening of the KARA storage ring as a function of absolute value of orbit offset is shown in Figure 3, where orbit length deviation due to COD misalignment errors is plotted by the blue curve, the contribution of betatron motion (beam size σβ) to the relative orbit lengthening is plotted by the red curve, and the IBS contribution to the orbit lengthening at high beam current, in this case 2.5 mA/bunch, is plotted by the green curve.

According to [33] the intra-beam scattering (IBS) at high current density and low beam energy leads to growth of beam emittance. The emittance of the KARA storage ring as function of beam energy is shown in Figure 4 taken from [33].

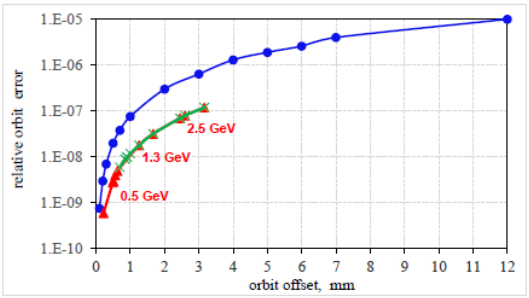

Figure 3: Relative orbit lengthening of the KARA storage ring as a function of absolute value of orbit offset: blue curve – contribution of COD errors, red curve – contribution of betatron motion (beam size σβ), and the green curve includes contributions of IBS into the emittance growth and orbit lengthening at high beam current 2.5 mA/bunch.

Simulations have been performed at "zero current" (see introduction), as well as at the high beam current of 2.5 mA/bunch. The DBA lattice was simulated using computer code ZAP [34].

Ring impedance was estimated as Z/n=2 Ohm. In Figure 4, the natural emittance at "zero current" (shown by open circles) is defined as the equilibrium between synchrotron radiation damping and heating due to quantum fluctuations. Natural emittance grows as the square of the relativistic factor $\epsilon x \sim \gamma 2$ from 2.4 nm at 0.5 GeV up to 58 nm at 2.5 GeV for TME mode, and from 3.5 nm up to 87 nm for DBA lattice.

At high beam current, the multiple small angle IBS contributes to the total growth rate in addition to quantum fluctuations. At injection energy of the KARA storage ring, the damping is slow (damping time is 0.3 s) and IBS growth rate exceeds damping speed. Equilibrium is reached at high values of beam emittance (~30 nmat 0.5 GeV), see green crosses in Figure 3 and black squares in Figure 4. Values of beam emittance contributed by IBS are outlined by numbers in blue in both Table 1 and Table 2.

At high energies above ~1.3 GeV, the damping rate of synchrotron radiation exceeds IBS heating, and beam emittance is then defined by the equilibrium between synchrotron radiation and quantum fluctuations. Even at large beam emittance and high current density, the contribution of betatron oscillations to the relative orbit lengthening should not exceed $(\Delta L/L)=10^{-8}$ at 0.5 GeV and 10^{-7} at 2.5 GeV, see red and green curves in Figure 3 as well as Table 1 and Table 2.

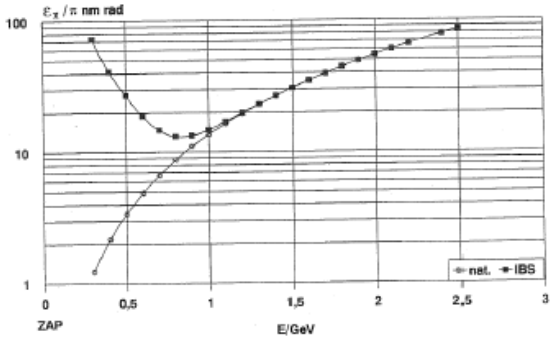

Figure 4: Beam emittance of DBA lattice of the KARA storage ring. Figure is taken from [19]. Circles – natural emittance at zero beam current, black squares – emittance at high beam current 2.5 mA/bunch including growth of beam size due to Intra-beam scattering. Ring impedance Z/n=2 Ohm. Simulations have been done by computer code ZAP [34].

Misalignment errors and orbit lengthening

Contribution of COD errors to the relative orbit lengthening does not depend on beam energy or on beam emittance. Pass length increases due to CODs include a few terms – the first two are caused by a quadratic angular error $x'cod^2$ in the horizontal plane, and $z'cod^2$ in the vertical plane, while a third contribution is caused by a quadratic term of orbit distortion inside the bends $xcod^2/\rho^2$, see equation (29)

$$\left(\frac{\Delta L}{L_0}\right)_{COD} = \frac{1}{2L_0}\oint\left(x'^2_{cod} + z'^2_{cod} + \frac{x^2_{cod}}{\rho^2}\right)ds \qquad 71$$

In order to estimate quadratic angular distortions, we analyze data from beam position measurements at a low positive compaction factor (Figure 5a), and compare it with results of computer simulations of orbit oscillations for off-momentum particles with a low compaction factor (Figure 5b).

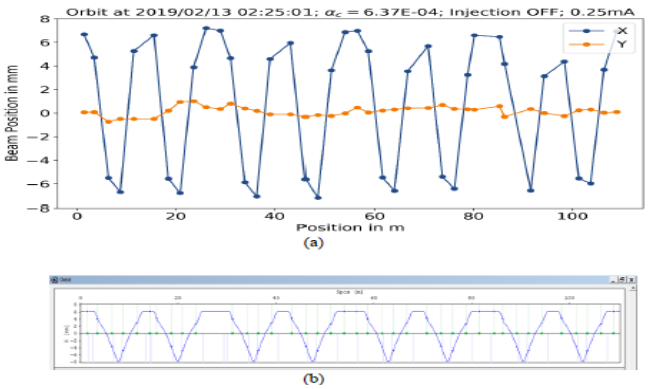

Figure 5: Orbit oscillations of beam in the horizontal plane of the KARA storage ring with low-α. Random position errors of magnets generate residual orbit lengthening and associated energy mismatching magnified by low-α: (a) measured data [16]; (b) Beam with energy offset δ = -0.5% (OPA simulations).

In experiments, and simulations, with low and negative compaction factors of the KARA storage ring, the orbit offset follows the pattern of the dispersion function where the ring lattice includes eight DBA sections. Contribution from angular quadratic errors was estimated by following equation

$$\frac{1}{2L_0}\oint\left(x'^2_{cod} + z'^2_{cod}\right)ds \cong \frac{1}{2L_0}\oint\left(\frac{x^{max}_{cod} - x^{min}_{cod}}{(76/16)}\right)^2 ds \cong 740\left(\frac{x^2_{cod}}{L_0^2}\right) \qquad (72)$$

Figure 5b takes into account that for the length of regions where orbit offset changes from a maximum positive value *xcodmax*, to a minimum negative value *xcodmin*, is slightly less than $L_0/16$. Because the orbit offset in the vertical plane is at least one order of magnitude less than radial offset, we neglect any contributions of vertical angular quadratic errors ($z'cod2 \approx 0$). Contribution from the quadratic term of orbit displacement, (*xcod*2), was estimated with an approximation of a constant orbit offset inside of the bending magnets

$$\frac{1}{2L_0}\oint\left(\frac{x^2_{cod}}{\rho^2}\right)ds \cong \frac{1}{2}\left(\frac{x^2_{cod}}{\rho^2}\right) \qquad (73)$$

The total contribution of orbit oscillations to the orbit lengthening of the KARA storage ring is given

$$\left(\frac{\Delta L}{L_0}\right)_{COD} = 740\left(\frac{x^2_{cod}}{L_0^2}\right) + 0.5\left(\frac{x^2_{cod}}{\rho^2}\right) \qquad (74)$$

The contribution of orbit misalignments due to COD errors to the relative orbit lengthening is summarized in Table 3 and shown by the blue curve in Figure 3.

Even at large beam emittance and high current density, the contribution of betatron motion into relative orbit lengthening should not exceed $(\Delta L/L) \approx 10^{-8}$ at 0.5 GeV and $(\Delta L/L) \approx 10^{-7}$ at 2.5 GeV, see red and green curves in Figure 3, as well as data from Tables 1, 2, 3. Orbit oscillations with an amplitude of more than 2 mm lead to a relative orbit lengthening $(\Delta L/L) > 5 \cdot 10^{-7}$. At low positive and negative momentum compaction factor operational modes, the span of orbit deviations exceeds ±2 mm (Figure 5). Orbit deviations due to COD errors are the main source of relative orbit lengthening in the KARA storage ring, especially at low and negative compaction factor operational modes.

Table 3: Contribution of orbit deviations due to COD errors to the relative orbit lengthening of the KARA storage ring

orbit offset	0.1 mm	0.2 mm	0.3 mm	0.5 mm	0.7 mm	1 mm	2 mm	3 mm	4 mm	5 mm	6 mm	7 mm	12 mm
$0.5\left(\frac{x_{cod}^2}{\rho^2}\right)$	$1.6.10^{-10}$	$6.4.10^{-10}$	$1.5.10^{-9}$	4.10^{-9}	8.10^{-9}	$1.6.10^{-8}$	$6.4.10^{-8}$	10^{-7}	$2.5\ 10^{-7}$	4.10^{-7}	6.10^{-7}	$9.\ 10^{-7}$	$2.3.10^{-6}$
$740\left(\frac{x_{cod}^2}{L_0^2}\right)$	6.10^{-10}	$2.4.10^{-9}$	$5.4.10^{-9}$	$1.5.10^{-8}$	3.10^{-8}	6.10^{-8}	$2.4.10^{-7}$	$5.4.10^{-7}$	10^{-6}	$1.5.10^{-6}$	2.10^{-6}	3.10^{-6}	9.10^{-6}
$(\Delta L/L_0)_{cod}$	$7.6.10^{-10}$	3.10^{-9}	7.10^{-9}	2.10^{-8}	$3.8.10^{-8}$	$7.6.10^{-8}$	3.10^{-7}	$6.4.10^{-7}$	1.310^{-6}	$1.9.10^{-6}$	$2.6.10^{-6}$	4.10^{-6}	$1.1.10^{-5}$

Stability Criteria and Limits Imposed On Free Momentum Independent Term (χ)

In order to estimate limits on the free momentum independent term (χ), one can simplify the full equation for orbit lengthening, equation (49) and neglect (at this moment only) the highest term of momentum compaction factor $a_3 \approx 0$. The solution of the reduced second order equation with a free term ($\chi \neq 0$) is [12, 21].

$$\alpha_2\delta^2 + \alpha_1\delta + \chi = 0 \qquad (75)$$

and it has two roots

$$\delta_{1,2} = \frac{1}{2\alpha_2}\left[-\alpha_1 \pm \sqrt{\alpha_1^2 - 4\alpha_2\chi}\right] \qquad (76)$$

Expression for synchrotron tune with an approximation of negligible third order term momentum compaction factor ($a_3 \approx 0$) is simplified to [18,21,35].

$$F_s = F_0 \sqrt{\frac{h_{rf}\, eU_{rf}(-cos\varphi_s)}{2\pi\beta_0^2 E_0}} \cdot \sqrt{\left[\frac{\alpha_1}{2} + \sqrt{\frac{\alpha_1^2}{4} - \alpha_2\frac{\Delta F_{rf}}{F_{rf}}}\right]} \qquad (77)$$

In general, a variation of RF frequency can be applied to compensate orbit lengthening due to coherent orbit errors. In this case, the free momentum independent term in equation (77) is substituted by a relative change of RF frequency $\left(\chi \approx \frac{\Delta F_{rf}}{F_{rf}}\right)$ [18,21,35].

Later we will show that in order to fit experimental results the expression for synchrotron tune should be expanded to second order in energy offset (δ^2) and the third order term of momentum compaction factor (α_3) must be included into the equation for (Fs), see equation (43) [4,5]. Stable fixed points in longitudinal phase space, i.e. buckets with bounded RF oscillations, exist if the roots of equation (76) are real numbers. This condition imposes an upper limit on (α2). Second order compaction factor must be less than.

$$\alpha_2 < \frac{\alpha_1^2}{4\chi} \qquad (78)$$

One should take into account that the free term is always positive ($\chi > 0$). From the upper limit on (α_2) defined by equation (76) it follows that at low compaction factor i.e. at $|\alpha_1| \sim 10^{-4}$ for the KARA storage ring, the coherent orbit errors, and betatron oscillations, should be limited to $\sqrt{x_{cod}^2 + x_\beta^2} \leq 1.5$ mm in order to reduce the momentum independent term to $\chi \leq 2 \cdot 10^{-7}$, and keep the second order term at $\alpha_2 \approx 10^{-2}$ "natural" level. Unfortunately, the KARA storage ring has no dedicated sextupoles for correcting the second order term of compaction factor independently from the chromaticity correction. Furthermore, from the second order equation (50), derived in approximation of a zero free term ($\chi = 0$), but including all three terms of momentum compaction factor, one can find the low limit of the second order term of compaction factor (α_2)

$$(\alpha_2^2 - 4\,\alpha_1 \cdot \alpha_3) > 0 \qquad (79)$$

Only a few options are available to realize this low limit condition:

- •If the first (α1) and the third (α_3) terms of compaction factor are of different signs, the second term is limited only from the upper side, see equation (78), and not from the low side. The absolute value of (α_2) can be as small as possible. It is the so called condition of zero longitudinal chromaticity;
- if the first (α_1) and the third (α_3) terms of compaction factor are of the same sign, then an absolute value of the second order compaction factor $|\alpha_2|$ cannot be reduced to less than $2\sqrt{\alpha_1 \cdot \alpha_3}$ see equation (79),
- For (α_1) and (α_3) terms of the same sign, the second order term (α_2) is strictly limited
- from the upper side by momentum independent residual errors x_{cod}^2 and x_β^2 and from
- the low side by the product of the first and third order terms

$$4\alpha_1\alpha_3 < \alpha_2{}^2 < \frac{\alpha_1^4}{16\chi^2} \qquad (80)$$

For example, at positive low-alpha optics $\alpha_1 = +1.04\times10{-}4$ with a third order term of opposite sign, $\alpha_3 = -0.259$, and a second term $\alpha_2 = +1.37\times10^{-2}$, the alpha-buckets could be observed if relative orbit errors are limited to $\chi < 3.6\times10^{-7}$ (corresponds to ≈2.5 mm). The magnitude of α_2 can be varied in a wide range in order to fit the energy gap between RF and α- buckets to the momentum acceptance of a ring.

At negative low -α optics, $\alpha_1 = -1.4\times10^{-4}$, with the third order term also of the same sign $\alpha_3 = -0.233$, and a second term $\alpha_2 = -2.1\times10{-}2$, the alpha-buckets might be realized if relative orbit errors will be limited to $\chi \leq 2.34\times10{-}7$ i.e. orbit misalignment due to COD errors should be limited to 1.7mm. In addition, in order to satisfy the stability limit in case where the first and third order

terms are of same sign ($\alpha_1 \cdot \alpha_3$) > 0, the absolute value of second term cannot be reduced to less than $|\alpha_2| \approx 1.2.10^{-2}$. Computer simulations with the orbit lengthening function fitted by a Polynomial of 5th order have confirmed that α-buckets just disappear if the absolute value of the second term is reduced to $|\alpha_2| < 1.4.10{-}2$.

It is still possible to fit an energy gap between RF and α-buckets to the momentum acceptance of a ring, but the value of the second order term might be varied only in a narrow range

$$-2.1\times10^{-2} \le \alpha_2 \le -1.2 \cdot 10^{-2} \qquad (81)$$

If the energy offset between RF and α-buckets stays within a momentum acceptance and the physical aperture of a ring, then a few simultaneous beams could be expected. At positive compaction factor, $\alpha_1 > 0$, and negative value of the third order term, $\alpha_3 < 0$, the strong limit, equation (79), on a minimum value of the second term α_2 is cancelled. At negative compaction factor ($\alpha_1 < 0$), phase space around a zero axes is reversed and RF buckets exchange their positions with off-momentum α-buckets.

Part 2: Applications of Theory to Existing Experiments

Based on theory described in Part 1, we would like to analyze and benchmark equations and theoretical predictions using experimental data from SOLEIL, as well as MLS [4, 8]. Also, we will estimate different features of low-α optics at the KARA synchrotron light source in order to increase the possibilities to build up α-buckets [16,30,31].

Analysis of Dedicated Experiments at The Soleil Ring

To benchmark simulations of α-buckets and check validity of equations (63), (64) and (65), we have chosen the same beam parameters as in the experiments at SOLEIL Light Source with nominal as well as with low-α optics, see [4, 36]. Numerical solutions of reduced quadratic equation (50), as well as full third order equation with a free term, equation (49), were compared and analyzed.

User Optics of the SOLEIL Ring

Parameters of momentum compaction factor terms $\alpha_1 = 4.38\times10^{4}$, $\alpha_2 = 4.45\times10^{-3}$ and $\alpha_3 = -3.95\times10^{-3}$, for nominal optics of the SOLEIL ring have been applied to find solutions of equations (63), (64) and (65). For small values of the relative momentum independent term ($\chi \le 10^{-7}$), three roots are real numbers. Two solutions from the third order equation ($\delta_2 = -8.95\%$, $\delta_3 = +121.6\%$) are exactly the same as roots of reduced quadratic equation (50). Also, the on-momentum root ($\delta_1 = 0$), corresponds to the reference orbit with nominal energy. The third order equation provides solutions which are complementary to solutions of a simplified second order equation. In addition, the third order equation allows to find momentum offset of orbits with a non-negligible momentum independent free term ($\chi \ne 0$).

Our simulations of nominal optics of the SOLEIL ring are well in agreement with results of SOLEIL simulations (Figure 6), giving three real roots ($\delta_1 = 0$, $\delta_2 = -9.1\%$ $\delta_3 = +122\%$) [4]. Real roots correspond to one on momentum RF bucket layer in longitudinal phase space with coordinates ($\varphi = \varphi_s$, $\delta_1 = 0$), i.e. stored beam, and two off-momentum alpha-buckets with coordinates ($\varphi = \pi - \varphi_s$, $\delta_2 = -8.95\%$) and ($\varphi = \pi - \varphi_s$, $\delta_3 = +121.6\%$). Previously described off-momentum α-buckets, are out of the SOLEIL transverse momentum acceptance (±4%) and therefore, out of the physical aperture of the ring. The beam cannot be stored in these α-buckets.

When the residual orbit errors are not negligible, and accordingly should be taken into account, the third order equation (49), including momentum independent term ($\chi \ne 0$), is applied in order to derive the roots i.e. momentum offset of RF and α-buckets in longitudinal phase space, see equations (63), (64), (65).

Benchmarking results of the influence of the momentum independent orbit errors and misalignments on the longitudinal phase space for SOLEIL, nominal optics are presented in Figure 6 [4]. All three buckets still exist, even at high relative coherent orbit offset up to ($\chi \approx 10^{-5}$), but their energy is shifted as shown in Figure 6. The on-momentum RF bucket (blue curve) located at phase (φ_s), is progressively off-centered from the reference orbit ($\delta_1 = 0$) to a momentum offset ($\delta_1 = -4.15\%$), while the energy independent term of relative orbit lengthening is increased from ($\chi = 10{-}8$) towards the high value ($\chi = 10^{-5}$). In contrary, the energy offset of α-buckets (red curve) is reduced in absolute value from ($\delta_2 = -8.95\%$) for a low level of COD errors ($\chi = 10^{-8}$), down to ($\delta_2 = -4.96\%$) for large error levels ($\chi = 10^{-5}$). Our estimations for nominal SOLEIL optics agreed well with results of SOLEIL simulations, which are depicted by black spots in Figure 6.

The RF and α-buckets are merged in energy, and stable motion disappears at a critical value of relative orbit displacement ($\chi = 1.2 \cdot 10{-}5$), corresponding to the amplitude of beam oscillations $\sqrt{x_{cod}^2 + x_\beta^2} \approx \pm 12\ mm.$ One real solution of a full third order equation still exists, large COD errors exceeding the critical value, are complex numbers ($\delta_{1,2} = -0.0456 \pm 0.0143$ i). Both stable fixed points and closed curves of elliptical shape around stable points are reversed to unstable points with saddle shape and hyperbolic open curves around it. Stable buckets disappear when beam motion is unstable. Results of our benchmarking estimations are well in agreement with SOLEIL coordinates of stable ($\delta_3 = +1.2194$) and unstable ($\delta_{1,2} = -0.0464 \pm 0.0114$ i) points for parameter ($\chi = 1.1 \times 10^{-5}$), see [3].

In 'real situation' when the orbit errors would exceed ($\chi > 8 \times 10^{-6}$), the energy offset of initially on-momentum RF buckets should exceed the momentum acceptance of SOLEIL lattice, and consequently the beam will be lost before reaching the critical point. According to estimations, see equation (72) and Table 3; the main contribution to the reversing of stable buckets into unstable, and visa-versa, comes from angular terms of orbit misalignment errors

$$(x'^2_{cod}).$$

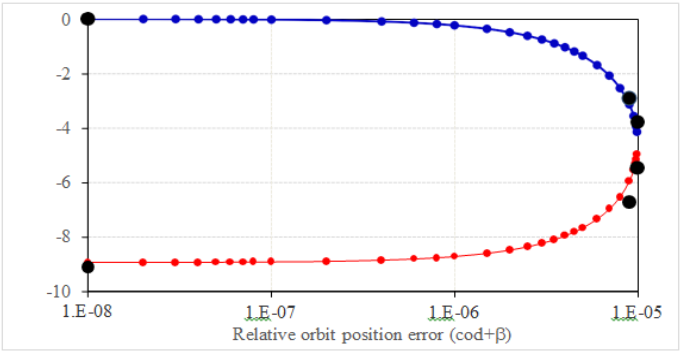

Figure 6: Benchmarking of the effect of the momentum independent orbit error (χ) on the longitudinal phase space for SOLEIL using nominal optics [4]. The on-momentum RF bucket (blue curve) is progressively off-centered from the nominal energy of reference orbit ($\delta_1 = 0$) to an orbit with momentum offset ($\delta_1 = -4.15\%$), while the relative orbit lengthening due to COD errors grows from ($\chi = 10^{-8}$) towards higher value ($\chi = 10^{-5}$). In contrary, the energy offset of off-momentum α-buckets (red curve) is reduced from ($\delta_2 = -8.95\%$) for small relative orbit errors ($\chi = 10^{-8}$) down to ($\delta_2 = -4.96\%$) for high values of orbit errors ($\chi = 10^{-5}$). Black circle spots depict results of SOLEIL simulations [4].

Simulations of Three Beams at Low-α Optics at SOLEIL

Three stable electron beams were simultaneously stored in the SOLEIL storage ring during low-alpha experiments; a mode in which the first term of momentum compaction factor was $\alpha_1 = 2.2 \times 10^{-5}$, the second term $\alpha_2 = -1.9 \times 10^{-5}$ and the third term $\alpha_3 = -9.3 \times 10^{-2}$, see Figure 7 taken from [3].

According to "The beams were imaged using a visible light monitor at a bending magnet exit port. The horizontal separation between the two side beams was measured to be 3 mm [4]. The streak camera bunch length measurements gave almost the same rms value of 4 ps for each of the beams at low current. This configuration was stable enough to enable injection directly in the three beams. It was then possible to ramp up the total beam current to 33 mA, distributed over 104 buckets. The total beam lifetime was 15 h." [4].

Using SOLEIL parameters for low-alpha optics we found numerical solutions for reduced quadratic equation (50), as well as for the full third order equation with a free term, equation
(49), and reproduced SOLEIL results at low-alpha optics with high accuracy. The effect of the momentum independent orbit error on the longitudinal phase space was investigated for the SOLEIL low-alpha optics, where the first term of momentum compaction factor is $a_1 = 2.2 \times 10^{-5}$, the second term $a_2 = -1.9 \times 10^{-5}$ and third term $a_3 = -9.3 \times 10^{-2}$.

The three stable beams, presented in Figure.7, were taken from [4]. The beams have been imaged using a visible light monitor at a bending magnet exit port where dispersion is ± = 10 cm, and distance between RF and α-buckets is ±1.5 mm. The spot in the middle of picture belongs to the bunches of nominal energy ($\delta_1 = 0$) located in the RF bucket, while the other two spots belong to bunches in the α-buckets with momentum offsets ($\delta_2 = +1.528\%$) and

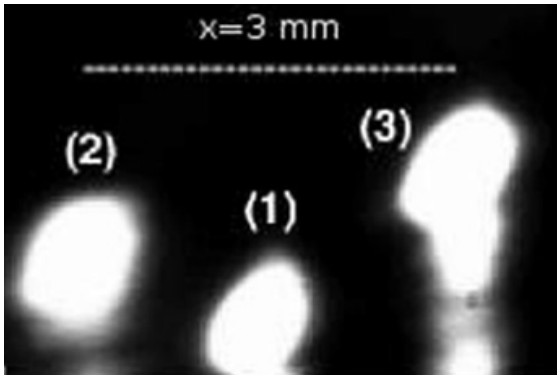

Figure 7: Images of three stable beams stored in the SOLEIL ring tuned to low-α optics. Spot (1) is referred to RF bucket, spots (2) and (3) are referred to α-buckets with momentum offset ±1.5%. Figure axes are vertical and horizontal beam positions. Dispersion at source position is $D = 10$ *cm.* The displacement in vertical plane is artifact of measurements. The image is taken from [4].

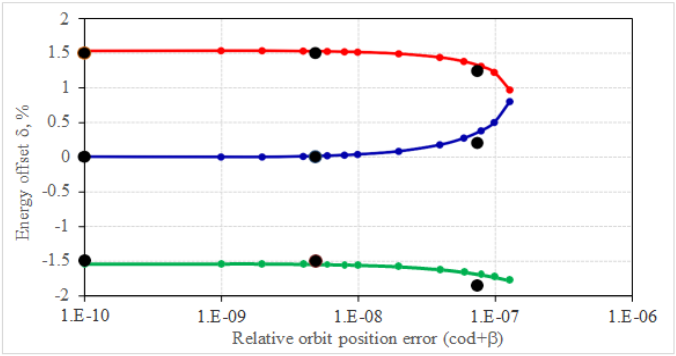

Figure 8: Effect of the momentum independent orbit error on the longitudinal phase space for the SOLEIL low-alpha optics. First term of compaction factor is $\alpha_1 = 2.2 \times 10^{-5}$, second term $\alpha_2 = -1.9 \times 10^{-5}$ and third term $\alpha_3 = -9.3 \times 10^{-2}$ [4]. The on-momentum RF bucket (blue curve) is progressively off-centered from the reference orbit ($\delta_1 = 0$) to the momentum offset ($\delta_1 = +0.8\%$). while the momentum independent term of relative orbit lengthening is increased from low ($\chi \leq 10^{-9}$) to large orbit errors ($\chi = 1.3 \times 10^{-7}$). The first off-momentum alpha bucket (red curve) reduces its energy offset from ($\delta_2 = +1.528\%$) at low orbit errors down to ($\delta_2 = +0.9\%$) at high value of orbit error. Second off-momentum alpha bucket (green curve) increases energy offset from ($\delta_3 = -1.548\%$) at low momentum independent term to ($\delta_3 = -1.78\%$) at large orbit errors. Black circle spots depict results of SOLEIL experiments taken from [4].

($\delta 3 = -1.548\%$). In order to evaluate SOLEIL experimental results, we have simulated the energy offset of RF and α-buckets at different values of misalignment errors using the third order equation (49), with free term (χ), see Figure 8. The on-momentum RF bucket (blue curve) is progressively off-centered from the reference orbit ($\delta_1 = 0$) for low levels of COD errors to different energy ($\delta_1 = +0.8\%$), while the momentum independent term of the relative orbit lengthening is increased from low ($\chi < 10^{-8}$) to high ($\chi = 1.3 \times 10^{-7}$) values of COD errors. The energy offset of a α-bucket with positive deviation in momentum (red curve) is reduced from ($\delta_2 = +1.528\%$) at low orbit errors ($\chi \leq 10^{-9}$) down to ($\delta_2 = +0.6\%$) at high COD errors ($\chi = 1.3 \times 10^{-7}$). The energy off-

set of alpha buckets with negative deviation in momentum (green curve) is increased in absolute value from ($\delta_3 = -1.548\%$) at small relative orbit errors ($\chi \sim 10^{-9}$) to ($\delta_3 = -1.78\%$) at high values of COD errors ($\chi = 1.3\times10^{-7}$). Black circle spots depict measured data taken from [4]. Results of our simulations agree well with SOLEIL results and provide a consistent explanation of beam energy offset with increased orbit off-centering.

Because the quadratic terms of misalignment errors cause oscillations of a beam around a reference trajectory, the orbit length, and average orbit radius, are different from the reference ideal orbit. As a consequence, the beam energy deviates from nominal value by

$$(\Delta E/E_0)_{COD} = \frac{1}{\alpha}\left(\frac{\Delta L}{L_0}\right)_{COD} \quad (82)$$

For 'user operation', when the value of momentum compaction factor is relatively high and dispersion function is always positive, one can compensate small energy offsets by variation of the RF frequency and center orbit. During low -α operation, energy offsets grow essentially even at small orbit misalignment and the amplitude of orbit oscillations at low -α is magnified by high values of a stretched dispersion function (Figure 5)

$$\Delta A_x = D_{max} \cdot (\Delta E/E_0)_{COD} \quad (83)$$

During low -α experiments at the KARA storage ring, beam orbit oscillations with span $\Delta Ax \approx \pm 8$ mm have been observed (Figure 5a). We've estimated the energy offset due to COD errors and misalignments to be as high as $\Delta E \approx$ -0.5% (Figure 5b).

Variation of Synchrotron Frequency with Energy Offset at SOLEIL
Variation of synchrotron frequency of an electron beam with respect to the relative variation in the RF frequency, have been measured at SOLEIL. Results are shown in Figure 9 (obtained from [4]). We have used already equation (43) to find the energy dependence of the synchrotron tune for up to the second order in momentum deviation (δ^2), and applied the same parameters as reported in: beam energy is 2.75 GeV, RF voltage -2.4 MV, RF frequency-352 MHz, RF harmonic number -416 [4]. Furthermore, the same values of compaction factor terms in the case of low-α optics have been chosen as well: $\alpha1=5\times10^{-6}$, $\alpha2=-1.8\times10^{-4}$ and $\alpha3=1.1\times10^{-1}$. Results of our simulations are shown in Figure 10. No stable α-buckets could be formed at these chosen values of momentum compaction factor. In order to convert momentum deviation with respect to the expected change of RF frequency, we applied a calculated relationship between the relative change of orbit length and that of the RF frequency variation,

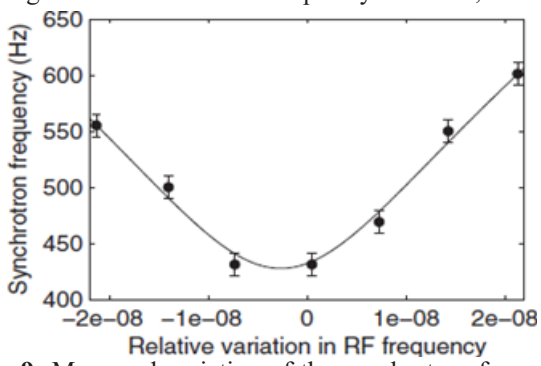

Figure 9: Measured variation of the synchrotron frequency with respect to the relative variation in the RF frequency. The dots are the measured data with their error bars of ±10 Hz. The solid curve corresponds to a fit of Eq. (77) expanded to the second order in momentum deviation (δ^2) in the case of a low -α optics: $\alpha_1=5\times10^{-6}$, $\alpha_2=-1.8\times10^{-4}$ and $\alpha_3=1.1\times10^{-1}$. Figure is taken from [4].

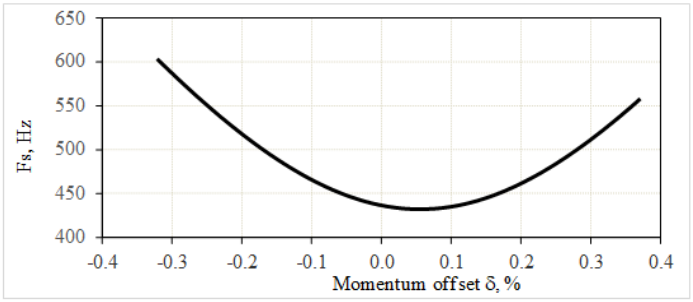

Figure 10: Synchrotron frequency (F_s) as function of momentum offset for SOLEIL low-α optics with $\alpha1=5\times10^{-6}$, $\alpha2=-1.8\times10^{-4}$ and $\alpha3=1.1\times10^{-1}$. Equation (43) was used for simulations.

where the relative orbit lengthening is expanded to third order in the energy offset

$$-\frac{\Delta F_{rf}}{F_{rf}} = \frac{\Delta L}{L_0} = (\alpha_3\delta^2+\alpha_2\delta+\alpha_1)\delta \quad (84)$$

The synchrotron frequency (FS) as function of RF frequency variation (dFrf) for SOLEIL low-α optics is plotted in Figure. 11 where results of simulations based on equation (43) are shown by black curve and experimental data are marked by blue circles with error bars. One can also apply an inverted polynomial and use equations (63, 64, and 65) where the free momentum independent term (χ) is substituted by a relative variation of RF frequency $\left(\frac{\Delta F_{rf}}{F_{rf}}\right)$ in order to convert frequency change (ΔF_{rf}) to momentum offset (δ). Our simulations based on equations (43) and (84) fit well to that of SOLEIL experimental data (Figure 9).

However, this was not true for the estimations of 'synchrotron frequency variation' with 'RF frequency change', based on the simplified equation (77), as this does not fit experimental data, see red curve in Figure 11 [18, 21, 35]. Only in one case, where the third order term of momentum compaction factor (α_3) is artificially zeroed in the full equation for synchrotron tune, equation, (43), did both equations produce the same result. The green dashed curve represents here the expected synchrotron tune in assumption that Fs would be dependent on α as expressed by formula (22) opposed to definition of Fs given in formula (43). It visibly deviates from experimental data.

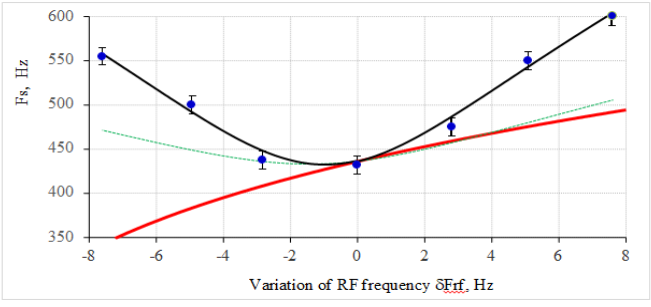

Figure 11: Synchrotron frequency as a function of RF frequency variation for SOLEIL with low α optics where $\alpha1=5\times10^{-6}$, $\alpha2=-$

1.8×10^{-4} and $\alpha3=1.1\times10^{-1}$. Black curve represents our simulations. Experimental data are marked by circles with error bars. Momentum deviation was converted into a variation of RF frequency using equation (84). The red curve depicts an attempt to fit the simplified equation (77) to data measured by SOLEIL. The green dashed curve represents here the expected synchrotron tune in assumption that Fs would be dependent on αas expressed by formula (22) opposed to definition of Fs given in formula (43). It visibly deviates from experimental data.

Benchmarking of low-α beams at Metrological Light Source

The Metrology Light Source (MLS) in Berlin, is a synchrotron radiation facility dedicated to metrology and scientific developments in the THz to extreme UV spectral range [37,38]. The MLS operates in the energy range from 105 to 630 MeV and is optimized for generating intense, broadband, coherent THz radiation, based on a bunch shortening low momentum compaction factor mode [39].

The MLS was the first electron storage ring to apply a combination of high order magnetic lenses (dedicated sextupole and octupole families) to correct second and third order terms of momentum compaction factor [5]. The beam is able to be directly injected into RF and/or α-buckets, and stored at positive or negative values of momentum compaction factor [8].

Parameters of RF and α-buckets at MLS

We calculated parameters of both RF and α-buckets from MLS in order to benchmark our simulations. High order terms of momentum compaction factors and energy gaps between RF and α-buckets of nominal, positive low -α, as well as negative low-α optics of the MLS ring are summarized in Table 4. Values of first, second, and third order terms of momentum compaction factor are taken from [8]. Momentum offsets of RF and α-buckets $\delta_{1,2,3}$ are estimated as roots (63,64,65) of the cubic equation (49), and compared with roots $\delta_{1,2,}$ equation (51) of the quadratic equation (50).

According to the dispersion function in 'user operational' mode of the MLS ring varies from Dmin=-0.2 m to Dmax=+1.5 m [8]. During operation at both low positive, as well as at negative compaction factors at MLS, the dispersion is stretched from Dmin=-1 m to Dmax =+1.9m.

Physical openings of the MLS vacuum chamber are less than the dynamic aperture of ring lattice, leading to a momentum acceptance of ±2.5% for 'user operation', and it is reduced to ±2% for low/negative -α operation. In theory, one can build up α-buckets at the MLS ring, even for user optics, because of the first (α_1) and third (α_3) terms of momentum compaction factor are of different signs and giving possible α-buckets being located at stable fixed points, see Table 4. Nevertheless, the absolute value of the third order term of alpha should be larger than $\| \alpha_3 \| > 90$ in order to reduce energy gap between RF and α-buckets to < ±1.5%, and fit both beams into the MLS acceptance (Table 4). At present MLS octupoles, with maximum excitation, can provide a third term of compaction factor of no more than $\| \alpha_3 \| < 16$. Moreover, phase space distortions due to octupole fields of high strength could destroy the dynamic aperture of a ring.

MLS measurements of simultaneously populated synchrotron radiation source positions associated with one RF (in the middle) and two α-buckets (left and right) are shown in Figure.12 (obtained [6,8]). MLS quadrupoles have been tuned for negative low-alpha optics with the first term of the momentum compaction factor $a_1 = -5 \times 10^{-4}$. The third term of compaction factor was fixed by octupoles to a positive value $a_3 = +4$, giving a longitudinal chromaticity of

$$\xi_s = \frac{dQ_s}{d\delta} \approx -\alpha_1 \frac{\Delta F_s}{\Delta F_0} = \frac{F_s}{F_0} \frac{(2\alpha_2 - \alpha_1^2)}{2\alpha_1}, \quad (85)$$

and used as the vertical axis of Figure.12 from -0.2 to +0.2, which corresponds to a change of the second order momentum compaction factor from $\alpha_2 = -4.4 \times 10^{-2}$ to $\alpha_2 = +4.4 \times 10^{-2}$. Vertical, horizontal and longitudinal sextupole families have been adjusted in order to keep transverse chromaticity unchanged during the scan. Dispersion was measured to be, D=0.3 m. The dashed black lines in Figure 12 shows the position of α-buckets estimated by equation $x_D = D\delta_{1,2}$. Here momentum offset $\delta_{1,2}$ of each α-bucket is a root, equation (51), of the second order equation (50). Similar measurements were performed at MLS by varying the first α_1 and third α_3 terms of momentum compaction factor, while reducing the second term to $\alpha_2 \approx 0$.

For simulation we reproduced the working points used for the MLS experiments and estimate the energy offset of α-buckets at negative low-α optics, with first term of momentum compaction factor $\alpha_1 = -5 \times 10^{-4}$ and third term $\alpha_3 = +4$, see (Figure13). The RF buckets are shown as a green line. The momentum deviation of α-buckets was calculated by a variation of the second term of compaction factor from a positive value $\alpha_2 = +4.4 \times 10^{-2}$ to a negative value $\alpha_2 = -4.4 \times 10^{-2}$.

Table 4: Parameters to benchmark the nominal, positive low-α and negative low-α optics of the MLS ring, including momentum independent coherent orbit distortion term χ

α_1	α_2	α_3	δ_1 (%)	δ_2 (%)	δ_3 (%)
nominal user optics					
$+3\cdot10^{-2}$	−0.38	−10	−7.7	+3.9	0
$+3\cdot10^{-2}$	−0.38	−30	−3.9	+2.6	0
$+3\cdot10^{-2}$	−0.38	−60	−2.6	+1.9	0
$+3\cdot10^{-2}$	−0.38	−90	−2.05	+1.6	0
low−α positive optics					
$+5.4\cdot10^{-4}$	$+5\cdot10^{-10}$	−4	−1.16	+1.16	0
$+1.3\cdot10^{-4}$	$+5\cdot10^{-3}$	−8.5	−0.42	+0.36	0
$+4.6\cdot10^{-4}$	$+1\cdot10^{-3}$	+3	UFP	UFP	0
$+1.0\cdot10^{-5}$	$+1\cdot10^{-2}$	+3	UFP	UFP	0
low−α negative optics					
$-5.4\cdot10^{-4}$	$-4.4\cdot10^{-2}$	+4	+1.84	−0.74	0
$-5.4\cdot10^{-4}$	$-2.4\cdot10^{-2}$	+4	+1.5	−0.9	0
$-5.4\cdot10^{-4}$	$-1\cdot10^{-5}$	+4	+1.16	−1.16	0
$-5.4\cdot10^{-4}$	$+2.4\cdot10^{-2}$	+4	+1.1	−1.3	0
$-5.4\cdot10^{-4}$	$+4.4\cdot10^{-2}$	+4	+1.1	−1.47	0

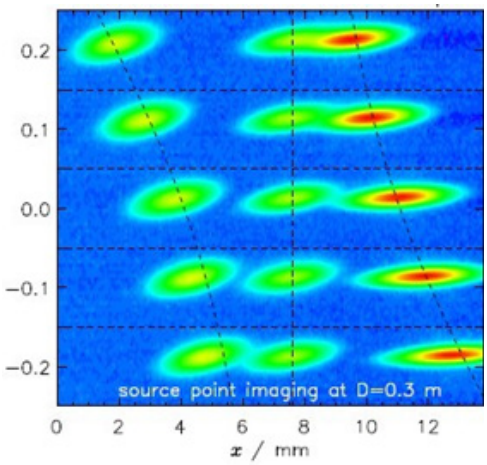

Figure 12: MLS measurements of simultaneously populated synchrotron radiation source position associated with one RF (in the middle) and two α-buckets (left and right). MLS quads have been tuned for negative low-α optics with the first term of momentum compaction factor $\alpha_1 = -5 \times 10^{-4}$. Longitudinal chromaticity was changed from +0.2 to -0.2 by variation of all three sextupole families in order to keep horizontal and vertical chromaticity unchanged. The third term of compaction factor was fixed by octupoles to a positive value $\alpha_3 = +4$. Dispersion was D=0.3 m. Figure was obtained from [6,8].

Results calculated using the quadratic equation (50) (shown as red curves with dots) are compared to the roots of cubic equation (49) (black curves with triangles). The momentum offsets of α-buckets for the MLS experiments were estimated by taking the difference between

the position of α-bucket and that of the RF bucket (reference orbit) and then converting it to an energy deviation $\delta_{1,2} = \frac{x_D}{D}$.

Results of MLS measurements are presented in Figure 13 by blue curves with squares [6]. Reduction of the momentum offsets of α-buckets from 1.8% down to 0.7% in Figure13 corresponds to a decrease of distance between RF and α-buckets from 7 to 3 mm in Figure 12. Momentum acceptance of the MLS lattice is limited at low -α optics to ±2% and three beams with energy offset up to ±2% can therefore be stored simultaneously. Results of benchmark simulations with an energy offset of α-buckets as a function of a high order terms of the momentum compaction factor, are in good agreement with experimental data and are within uncertainties of experimental conditions. Roots of the third order equation (49) should always be checked for consistency with roots of the simplified second order equation (51). Both equations are complementary to each other.]

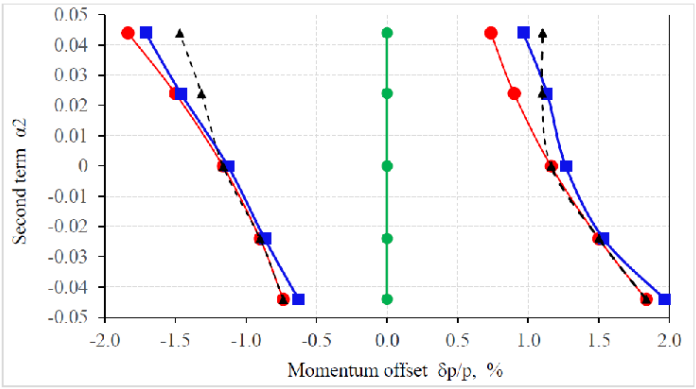

Figure 13: Simulations of energy deviation of α-buckets with respect to a RF bucket (green line). The momentum offset of α-buckets was changed by variation of the second term of the compaction factor from $\alpha_2 = +4.4 \times 10^{-2}$ to $\alpha_2 = -4.4 \times 10^{-2}$ corresponding to a change of longitudinal chromaticity from -0.2 to +0.2. Dispersion was D=0.3 m at the observation point. Calculations using the quadratic equation (50) are shown by the red curve, calculations using the cubic equation (49) are given in black, and measured data in blue [6].

Simulations of Synchrotron Tune Variation Based On MLS Experiments

Synchrotron frequency of an electron beam as a function of RF frequency variation has been measured at the MLS ring; the results are shown in Figure 14 (obtained from [5]). All three families of the MLS sextuples have been tuned to minimize longitudinal chromaticity to ξs ≈ while horizontal and vertical chromaticity's were fixed at slightly positive values $\xi_{x,y} \leq 0.2$. The value of synchrotron frequency, $F_r = 9.5$ kHz, for on-momentum particles ($\Delta F_{rf}=0$), was measured and corresponds to a compaction factor $\alpha_1=+4.6\times10^{-4}$.

Octupoles control the curvature of synchrotron tune, F_s, with respect to the variation of RF frequency, ΔF_{rf}. Referring to Figure 14, the almost flat curve marked "B" represents the case when octuplets are "off". The curve marked "C" shows the synchrotron tune when octuplets were switched "on". The value of third term of compaction factor α3=+3 was estimated by a fit [5].

We reproduced measurements of synchrotron tune made at MLS, and then calculated the synchrotron tune as a function of energy deviation, while applying equation (43) with a momentum offset up to second order (δ^2). Results of our simulations are shown in Figure 15. According to, the beam energy is 630 MeV, RF voltage - 250 kV, RF frequency - 500 MHz and RF harmonic number is 80 [5]. Values of the first and third compaction factor terms were chosen the same as used in the MLS experiments, namely $\alpha_1=4.6\times10^{-4}$

and α_3=+3. The value of the second term, $\alpha 2=+10^{-3}$, is a result of our fit which produces a slight tilt of the measured curve shown in Figure 14. Positive values of the first and third term products, (α_1. α_3>0), used in the experiments prevent the formation of stable α-buckets, similar to SOLEIL measurements of synchrotron tune (Figure 9). We benchmarked our simulations (Figure 16) with MLS results and converted the momentum deviation to the change of RF frequency using the relationship between the relative deviation of orbit length and the RF frequency variation (84); where orbit length is expanded to the third order in energy offset. Results of MLS measurements are marked by blue squares in Figure.16 while results of simulations based on equations (43) and (77) are shown by black curve. The green dashed curve represents here the expected synchrotron tune in assumption that Fs would be dependent on α as expressed by formula (22) opposed to definition of Fs given in formula (43). It visibly deviates from experimental data. Results of simulations based on equations (43) and (84) precisely fit to that of MLS experimental data (Figure.14).

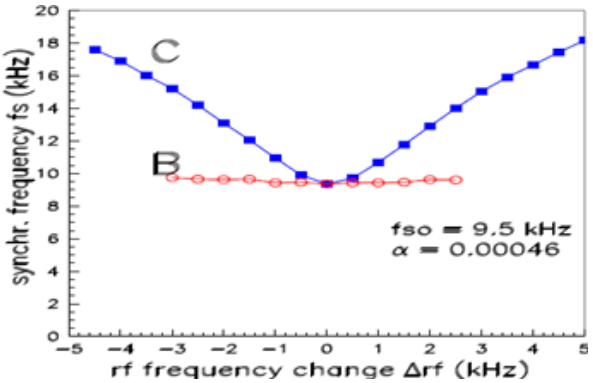

Figure 14: Synchrotron tune as a function of RF frequency variation, measured at MLS: case "B"- strength of all sextupole families were adjusted to minimize longitudinal chromaticity while octupoles were "off"; case "C"- octupoles were excited in addition to sextupoles in order to create a positive curvature of synchrotron tune. Figure obtained from [5].

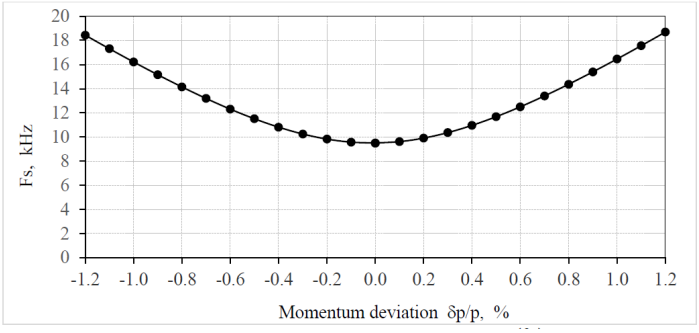

Figure 15: Synchrotron tune (Fs) as a function of momentum offset $\left(\frac{\delta p}{p_0}\right)$. Simulation of MLS low-α optics with α_1=+4.6×10^{-4}, α_2=+10^{-3} and α_3=+3. Calculations have been done using equation (43)

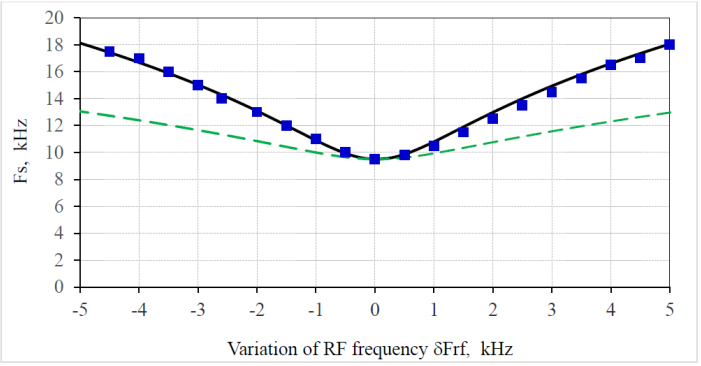

Figure 16: Simulations of synchrotron tune as a function of RF frequency variation for MLS low-α optics with α_1=+4.6×10^{-4}, α_2=+10^{-3} and α_3=+3. Momentum offset was converted into a variation of RF frequency using equation (84), with high order terms of momentum compaction factor. Experimental data are marked by blue squares while results of simulations based on equations (43) and (84) are shown by black curve [5]. The green dashed curve represents here the expected synchrotron tune in assumption that Fs would be dependent on α as expressed by formula (22) opposed to definition of Fs given in formula (43). It visibly deviates from experimental data.

Estimation of Beam Life-tTime During low-α experiments at MLS ring

We came to the conclusion that benchmark simulations, using the equation for synchrotron tune with high order terms of momentum offset (43), and converting the momentum offset to a variation of RF frequency (84), are well fitted to experimental data from independent experiments at both MLS and SOLEIL, and can be used to describe details of longitudinal beam dynamics [3,5,8].

In the following, we propose a consistent explanation of lifetime effects based on the results of MLS experiments at different low-α settings and octuplets current, see Figure 17 (obtained from [5,8]. "For a multi-bunch beam of approximately 15 mA at 630 MeV energy and 250 kV RF voltage, the life-time was measured for different excitation currents of the octupoles from -6 A to +6A" [5]. According to MLS experiments, without octuplets powered with negative current, then values of synchrotron tune less than $F_s < 7$ *kHz* cannot be reached. For evaluation, the second term of momentum compaction factor was reduced to approximately zero by sextupoles. Then the scan of the octupole current over its full range was performed and life-time was measured [8]. Measurements have been repeated for different values of positive momentum compaction factors ranging from 1.15.10^{-3} down to 4.5.10^{-5}. For a positive value of the third term of momentum compaction factor α_3>0 (corresponds to negative current of octupoles in Figure 17) life time is stable. For every α_1 there is a certain octupole current, where the lifetime starts to decrease drastically" [8].

Beam losses of high energy electrons in storage rings depend on

different factors, for example: multiple elastic scattering of electrons, but on small angles is suppressed by synchrotron damping; multiple small energy losses due to inelastic scattering, but can be compensated for by RF; single large amplitude elastic (vacuum losses) and inelastic (Bremstrahlung effect) scattering of electrons on atoms and molecules of residual gas and finally, large angle scattering of electrons on each other inside the bunch (Touschek effect) [40-48]. The intra-beam scattering contributes to emittance growth at low beam energies and high beam current [34]. Large angle scattering effects limit the beam life-time in light sources. In general, the loss rate due to Touschek effect is dominant at low beam energies as well as at high beam densities.

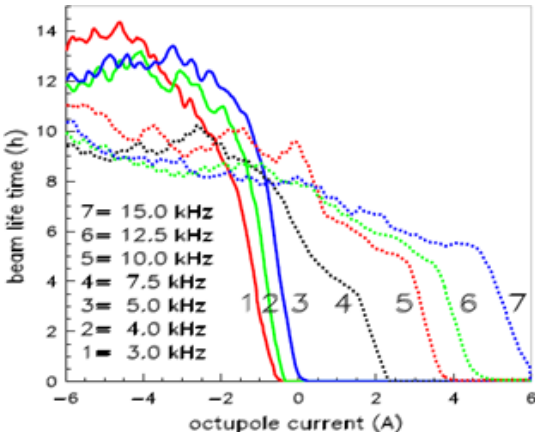

Figure 17: Life-time of 630 MeV beam as a function of octupole current and different low-α values measured at MLS experiments. RF voltage is 250 kV. Without octupoles powered with negative current, values of synchrotron tune $F_s < 7\ kHz$ cannot be reached. Figure is taken from [5,8].

The rate of beam losses due to elastic scattering is inversely proportional to the physical aperture of the vacuum chamber, or dynamic aperture, whichever is less [49,50]. The rate of beam losses caused by single inelastic scattering is inversely proportional to the momentum acceptance of a ring [51,52]. Beam losses are reduced and life-time is improved when the momentum acceptance is large [53].

In order to describe results of life-time measurements at MLS we estimated the momentum acceptance of the MLS ring for different operational conditions (Fig. 17, numeration of curves is given in the first row of Table 5.). The ring lattice limits momentum acceptance to 2.5% in 'user operation' mode and to ~2% at low -α conditions [8]. RF momentum acceptance, defined as the height of an RF bucket, is limited by the square root of the RF voltage amplitude [12,13], and can be found from

$$MA_{RF} = \delta_{max} = \pm \sqrt{\frac{2\,eU_{rf}}{\pi h_{rf}\,\beta_0^2 E_0}\left[cos\varphi_s - \left(\frac{\pi}{2} - \varphi_s\right) sin\varphi_s\right]} \cdot \sqrt{\frac{1}{\alpha_1}} \qquad (86)$$

For 'user operational' mode, with a beam energy of 630 MeV and RF voltage at 250 kV, the bucket height of the RF system limits the maximum momentum offset of particles captured by the RF bucket to $MA_{RF} = \pm 1\%$, this is due to the high value of momentum compaction factor $\alpha 1 = 0.03$. But at low values of compaction factor, MARF is increased to ±5% at $\alpha_1 = 10^{-3}$ and to ±17% at $\alpha_1 = 10^{-4}$. From this one must conclude that other physical effects are responsible for the reduction of life-time in MLS experiments.

In the presence of α- buckets, one could assume that the energy gap (δ) between RF and α- buckets limits the momentum acceptance of a ring. Indeed, in equations (51, 63, 64 and 65) α- bucket layers are shifted in energy with respect to reference orbit. Unstable fixed points of on-momentum RF bucket (separatrix "saddle") are located at the same phase (π − φs) as where the stable fixed points ("focus") of α- buckets are located. Thus, bucket height cannot be larger than the energy gap between RF and α- bucket. Nevertheless, one may propose an even stronger limit based on non-linear behavior of synchrotron tune.

We've calculated synchrotron tune as a function of the momentum offset at different settings of low -α optics of the MLS ring using equation (43) with high order terms of momentum compaction factor. Parameters of low -α optics and synchrotron tune are summarized in Table 5. According to, during experiments all three sextupole families have been adjusted to minimize the second term of momentum compaction factor (α_2), and fix transverse chromaticity [8]. We've checked different values of (α_2) and found no significant difference in the final results for any small value less than ($\alpha_2 < 10^{-3}$). Thus, the value of the second term ($\alpha_2 = 10^{-4}$) was chosen for our benchmarking estimations. The semi-empirical equation derived by M. Ries from direct Compton backscattering measurements of low -α compaction factor was used to convert octupole current into the expected value of the third term of compaction factor (α_3) [8].

$$\alpha_3 \approx -3 - 2I_{oct} \qquad (87)$$

"Natural" curvature of MLS low -α optics without octupoles, $\alpha_3(I_{oct} = 0) \approx -3$, was predicted by MAD-X simulations and confirmed by measurements [8]. For each value found for the first term of compaction factor (α_1), presented in Table 5, we applied equation (43) and estimated synchrotron tune (F_s) as a function of the third term (α_3). Fig. 18 shows the Synchrotron tune (F_s) as a function of the momentum offset of particles in a beam; a low-α

Table 5. Parameters of low -α optics to reproduce MLS life-time experiments [5,8].

curve	1	2	3	4	5	6	7
F_s, kHz	3	4	5	7.5	10	12.5	15
α_1	$4.5\cdot10^{-5}$	$8.2\cdot10^{-5}$	$1.3\cdot10^{-4}$	$2.9\cdot10^{-4}$	$5.1\cdot10^{-4}$	$8\cdot10^{-4}$	$1.15\cdot10^{-3}$
α_2	10^{-4}	10^{-4}	10^{-4}	10^{-4}	10^{-4}	10^{-4}	10^{-4}
α_3	-1	-2	-3	-6.6	-10	-13	-16
I_{oct}, A	-1	-0.5	0	+1.8	+3.5	+5	+6.5

operation mode with (α_1=+1.3·10-4) was chosen as an example. As the third term of momentum compaction factor (α3) was varied from -3 to +4, the curvature of function FS (δ) changes from a "natural" negative value to a positive value. At ($\alpha_3 \approx 0$), the non-linear dependence of synchrotron tune on the momentum offset has almost vanished, see "brown" curve in Fig. 18. Without octupoles ("red" curve with (α_3=-3), the synchrotron tune sharply drops to zero at a value of momentum offset of only ($\delta_{(FS=0)} = \pm 0.38\%$). This value is a few times less than the MLS acceptance defined by the ring lattice ($MA_{LAT} \approx \pm 2\%$), and it is essentially less than the expected energy gap between RF and α- buckets ($\delta\alpha = \pm 0.66\%$) estimated by the equation (51).

We assume that the reduction of synchrotron tune to almost zero has led to longitudinal instability and loss of a beam as described in experiments earlier. In the 630 MeV energy range, the equilibrium energy spread of the MLS beam is $\delta p = 4.4 \cdot 10^{-4}$ (rms), and particles on the periphery of the Gaussian distribution (beam "halo"), hit a stability limit (Fs ≈ 0) and will be lost. In our chosen example, with octupoles powered by small negative current (I_{oct}=-1 A), the third term of the compaction factor is reduced to (α_3=-1). Consequently, the synchrotron tune (blue curve in Fig. 18) still drops to zero, but at a higher value of momentum offset, namely at ($\delta_{(Fs=0)} = \pm 0.64\%$) and the life-time is improved. When powering the octupoles with a high negative current, the curvature of the synchrotron tune function is positive, and the life-time

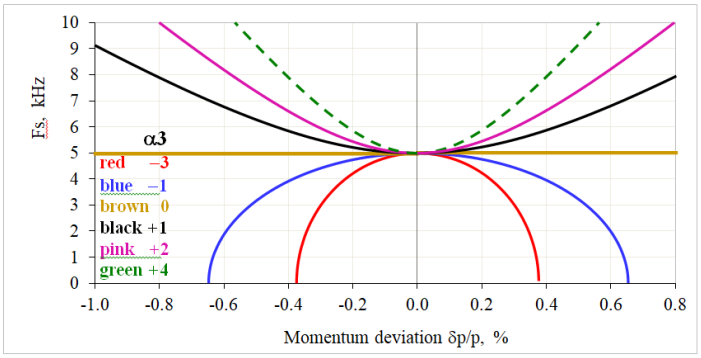

Figure 18: Synchrotron tune (Fs) as a function of the momentum deviaton of particles in a beam from a reference orbit energy. Low -α operation mode with (α_1=+1.3·10^{-4}) at the MLS ring was chosen as an example. The third term of momentum compaction factor (α_3) was varied from -3 to +4 depends on other factors. Our simulations precisely correlate with the MLS experiments where a synchrotron tune less than Fs ≤ 5 kHz cannot be reached without octupoles powered with negative current.

For each curve plotted in Fig. 17, we estimated experimental values of octupoles current for when the life-time starts to drop, and then converted the octupole current to values of the third order term (α_3); parameters can be found in Table 5. These converted values of (α_3) are used to calculate the synchrotron tune as a function of the momentum offset for each curve of Fig. 17. Results are shown in Fig. 19. At higher values of the first term (α_1), the curvature (α_3), of the compaction factor function α(δ), should be increased in order to fit approximately to the same limit of the momentum offset where life-time starts to decrease. During MLS experiments the octupole current has been gradually increased for higher values of compaction factor (α_1) and the curvature of the compaction factor was increasing. The transition point corresponds to $\delta_{(Fs=0)} \approx 0.5\%$, as can be seen in the example above, see Fig.19.

For a particular case of low -α optics when the first and third terms of the compaction factor are of different signs, and its product is always negative ($\alpha_1 \cdot \alpha_3 < 0$), one could estimate a momentum acceptance applying the condition of zero synchrotron tune ($F_s = 0$). The following equation is based on equation (43) for a synchrotron tune as a function of high order terms of momentum offset

$$3\alpha_3\delta^2 + 2\alpha_2\delta + \alpha_1 = 0 \qquad (88)$$

Roots of equation (88) define the condition of zero synchrotron tune and maximum acceptable

$$MA_{(Fs=0)} = \delta_{(Fs=0)} = \frac{1}{3\alpha_3}\left[-\alpha_2 \pm \sqrt{\alpha_2^2 - 3\alpha_1\alpha_3}\right] \qquad (89)$$

energy offset of particles in a beam. Limits on momentum deviation, imposed by the synchrotron tune, can be a few times less than the momentum acceptance defined by the energy gap between RF and α- buckets, or by the ring lattice and RF bucket height. For a case of minimized second term (α_2=0), as well as first and third order α- terms of different signs ($\alpha_1 \cdot \alpha_3 < 0$), the momentum acceptance limited by synchrotron tune $MA_{(Fs=0)} \approx \pm\sqrt{-\frac{\alpha_1}{3\alpha_3}}$ is $\sim\sqrt{3}$ times less than limits imposed by the energy gap between RF and α-buckets $MA_{(\alpha=0)} \approx \pm\sqrt{-\frac{\alpha_1}{\alpha_3}}$

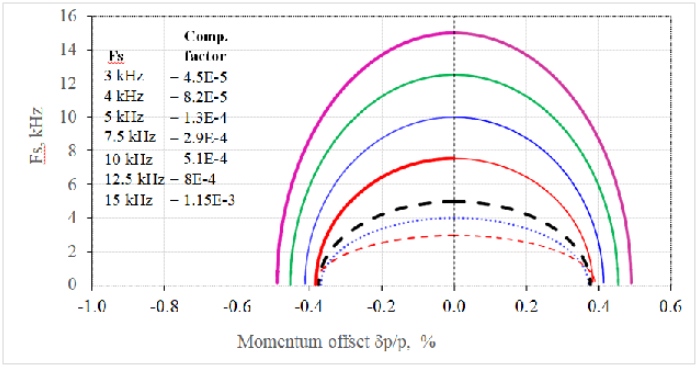

Figure 19: Synchrotron tune (Fs) as a function of momentum offset for low -α operation modes ranging from (α_1=+4.5·10^{-5}) to (α_1=+1.15·10^{-3}). Values of the third term of momentum compaction factor (α3) were adjusted for each curve individually, see text.

Part 3. Studies of α- buckets at the KARA storage ring

The KARA electron storage ring (former ANKA ring) operates in the energy range from 0.5 to 2.5 GeV. In order to improve machine performance, the comprehensive studies and precise modelling of linear and nonlinear optics have been performed [55]. In this framework, the higher order momentum compaction factor has been determined exploiting the extraordinary precision of the resonant spin depolarization method [56].

Benchmarking of KARA Experiments

Detailed studies have been carried out for the former ANKA ring optics version with moderately reduced momentum compaction factor, not far away from the threshold of observation of coher-

ent synchrotron radiation [54]. In order to estimate the high order terms of momentum compaction factor, the frequency of synchrotron oscillations was measured with a strip-line as a function of the RF frequency [55]. Measured values for the synchrotron frequency Fs at different RF frequencies are plotted in Fig.20 taken from [56]. Variation of RF frequency $\Delta F_{rf}/F_{rf}$ is shown relative to the central RF frequency F0. The deviation from a linear behavior is found to be highly significant. The value of synchrotron frequency, Fs = 8.7 kHz, for on-momentum particles (ΔFrf = 0), was measured and corresponds to a momentum compaction factor α_1=+4.84x10^{-4}. We've reproduced values of the measured synchrotron tune at KARA, and then calculated the synchrotron frequency as a function of energy deviation, while applying equation (43) with a momentum offset up to second order (δ^2), see Fig.21.

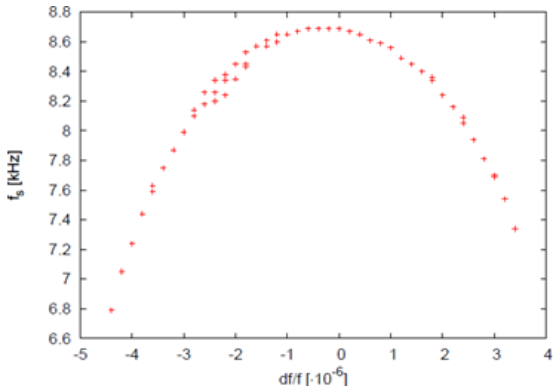

Figure 20: Measured values for the synchrotron tune Fs at KARA at different RF frequencies $\Delta F_{rf}/F_{rf}$ (shown relative to the central frequency F0). Figure is taken from [56].

The blue curve in Fig.21 represents results of our simulations. According to [56], RF frequency is 500 MHz and RF harmonic number is 184. Value of the first term of low compaction factor term was chosen the same as was measured in the KARA experiments, namely α_1 =4.84x10^{-4}. Values of second term α_2=+5.5x10^{-2} and third term α_3= -70 terms is a result of fit to experimental data marked by black circles in Fig.21. The red dashed curve represents here the expected synchrotron tune in assumption that Fs would be dependent on α as expressed by formula (22) opposed to definition of Fs given in formula (43). It visibly deviates from experimental data.

One should mention here that estimated value of the third term is excessive in comparison with "natural" value of α_3~-0.6 from computer simulations of non-linear low -α KARA optics. Octupoles components of magnetic elements of KARA ring are small and can't contribute to

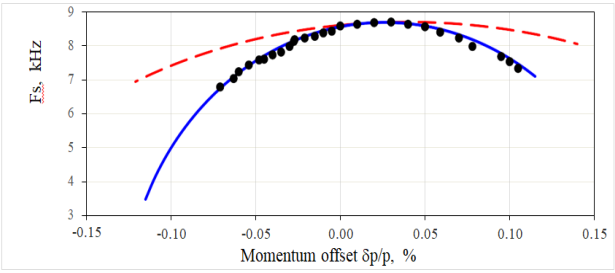

Figure 21: Synchrotron tune (Fs) as a function of momentum offset Equation. Equation (43) with first term of momentum compaction factor α_1=+4.84x10^{-4} has been applied for simulations (blue curve). Values of second α_2=+5.5x10^{-2} and third α_3=-70 terms is a result of fit to experimental data (marked by black circles). The red dashed curve represents here the expected synchrotron tune in assumption that Fs would be dependent on α as expressed by formula (22) opposed to definition of Fs given in formula (43). It visibly deviates from experimental data.

Such a high value of third term of momentum compaction factor. Same is valid for other rings, for example MLS ring, in case if dedicated octupole lenses are not applied, see Tables 4 and 5. Similar fit of KARA experimental data but only for one branch of the synchrotron tune curve was performed for same first term of momentum compaction factor α_1=+4.84x10-4 but slightly modified second order term α_2=+1.2x10^{-1} and natural value of third term α_3 = -0.55. Estimated value of the second term is close to fit of α_2= (9.81±0.25)·10^{-2} of curve at Fig.20 [56].

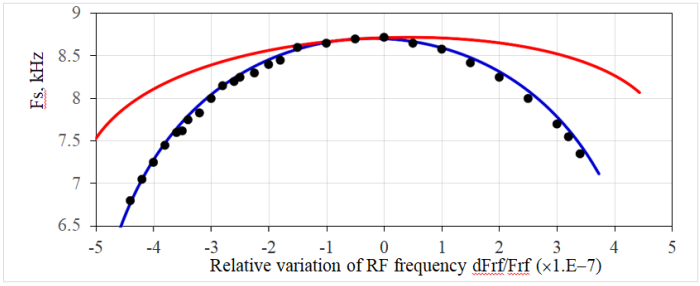

a

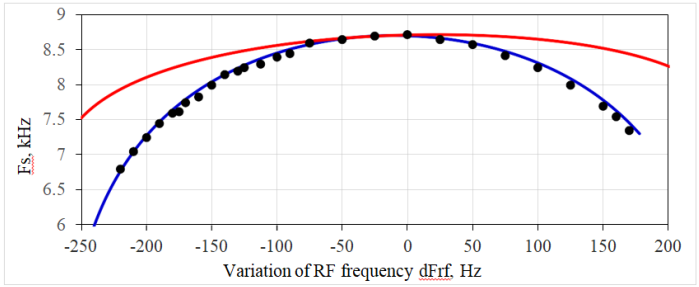

b

Figure 22: Synchrotron frequency of KARA as a function of variation of RF frequency: (a) (Fs) versus relative change of RF frequency (dFrf/Frf); (b) (Fs) as a function of RF frequency (Frf) variation. Simulations of low -α optics where α_1=4.84x10^{-4}, α_2=+5.5x10^{-2} and α_3= -70 are presented by blue curve. Experimental data are marked by black circles. Momentum deviation was converted into a variation of RF frequency using equation (84). The red dashed curve represents here the expected synchrotron tune in assumption that Fs would be dependent on α as expressed by formula (22) opposed to definition of Fs given in formula (43). It visibly deviates from experimental data.

Also our estimations of all three terms of momentum compaction factor are similar to main and high order coefficients of alpha, namely, α_1= (4.7±0.2)x10^{-4}, α_2= (1.6±0.4)x10^{-1} and α_3= -(2±1.6) derived from precise determination of the electron beam energy with Compton backscattered laser photons at ANKA, see Fig. 6.18 of [57].

We've performed reversed transformation of Cardano equations (63), (64), (65) with same momentum compaction factor terms in order to derive expected values of momentum offset ($\delta p/p_0$) and corresponding values of synchrotron tune (Fs). For that the free momentum independent term (χ) was substituted by relative variation of RF frequency (dFrf/Frf).

Results are well fit to blue curve shown in Fig. 21. Positive value of the first term ($\alpha_1>0$) and negative value of the third term ($\alpha_3<0$) would allow the formation of stable α-buckets ($\alpha_1\cdot\alpha_3>0$) at these specific settings of momentum compaction factor. By substituting high order terms of momentum compaction factor to equations (51) as well as (63), (64), (65), we've estimated energy offset of expected α- buckets at KARA tests as δ_2=+0.396% and δ_3= -22% (out of ring momentum acceptance).

We've benchmarked our simulations with KARA results and converted the momentum deviation to the change of RF frequency using the relationship between the relative deviation of orbit length and the RF frequency variation (84); where orbit length is expanded to the third order in energy offset. Synchrotron frequency of KARA vs RF frequency is shown in Fig.22. The synchrotron tune (Fs) as function of relative change of RF frequency (dFrf/Frf) is presented at Fig.22a. The synchrotron tune (Fs) as a function of RF frequency (Frf) variation is shown in Fig. 22b. Results of low -α optics tracking where $\alpha_1=4.84\text{x}10^{-4}$, $\alpha_2=+5.5\text{x}10^{-2}$ and α_3= -70 are presented by blue curve. Experimental data are marked by black circles. Momentum deviation was converted into a variation of RF frequency using equation (84). The red dashed curve represents here the expected synchrotron tune in assumption that Fs would be dependent on α as expressed by formula (22) opposed to definition of Fs given in formula (43). It visibly deviates from experimental data.

KARA Model and Beam Parameters

In order to fill and store beam in α- buckets one should precisely define parameters of ring elements, influencing position and energy shift between RF and α- buckets. In case of KARA light source, we determined parameters of α- buckets based on known dispersion, strength of quadrupoles and sextupoles and derived expected momentum offset, energy acceptance and life time of α- buckets.

Parameters of α- buckets at the KARA storage ring have been estimated based on second order equation (50) and third order equation with a free term (49), and compared with results of computer simulations. A computer model of the storage ring, booster ring, and injection line is shown in Fig.23. The model includes all elements with real apertures, namely: vacuum chamber, bending magnets, quadrupoles, sextupoles, correctors, kickers, septum, insertion devices, scrapers etc. [29,30]. High field superconducting wigglers CATACT and CLIC, as well as the superconducting undulator SCU20, are approximated by linear models and shown by long green strips in Fig.23. High order components of magnetic field perturbations, in particular, the residual octupole components of the high field superconducting wigglers, are treated as thin multipole lenses [31].

The computer code OPA was used to simulate the storage ring lattice, dynamic aperture, momentum acceptance and other non-linear features of a beam in transverse planes [58]. Furthermore, to study the longitudinal phase space, namely, the orbit lengthening, linear and high order terms of momentum compaction factor etc. For a realistic estimation of beam dynamic effects, the parameters of the ring model were chosen close to the measured one (Table 6).

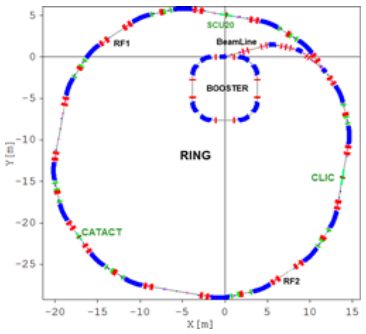

Figure 23: Model of the KARA storage ring, booster ring and injection line [30,31]. Bending magnets are depicted in blue, quadrupoles in red and sextupoles are marked in green. Wigglers are shown by long green strips.

Table 6. Model parameters of KARA storage ring and beam

Parameter	KARA	
Energy	0.5÷2.5 GeV	
Circumference, m	110.4	
Chromaticity $\xi_{X,Y}$	+1 (α>0) / -1 (α<0)	
Hor/vertical tunes QX / QY	6.761 / 2.802	
RF frequency / harmonic	500 MHz / 184	
Vacuum and gas composition-as	10^{-9} tor, Z=7, A=2, 10%CO+H_2	
RF voltage, MV	≤1.6	
Lattice momentum acceptance	2% (user)	1% (low-α)
Current per bunch	0.1÷1 mA	
Damping time (hor/vert/long) ms	380/370/180	0.5 GeV
	3/3/1.5	2.5GeV
Energy loss due to synchrotron radiation	1 keV/turn	0.5 GeV
	622 keV/turn	2.5GeV
Natural energy spread	$1.8\cdot10^{-4}$	0.5 GeV
	$9\cdot10^{-4}$	2.5GeV

According to theory, as well as to MLS [8] and SOLEIL [4]studies, α-buckets are shifted in energy causing them to be off from the reference orbit. Sufficient momentum acceptance is required to accommodate both RF and α- buckets in a storage ring. Many light sources, like: DIAMOND [7], SOLEIL [59], MAX–IV 3 GeV ring [60], NSLS-II [61], SLS-2 [62], BESSY- II [63], ESRF [64] etc. have incorporated low dispersive lattices with the purpose to realize low emittance beams, large momentum acceptance and improved beam life-time. In the ideal case, the dynamic aperture should be larger than the geometric acceptance defined by dimensions of vacuum chamber, insertion devices, collimators, scrapers etc. Nevertheless, at certain conditions the momentum acceptance of the KARA storage ring is limited by non-linear features of ring

optics (Fig.24). For a 'user operational' mode of KARA (Fig.1), and 2.5 GeV energy range, the momentum acceptance of ring lattice is further reduced by the small size of RF buckets (±1%). At present, the maximum available amplitude of RF voltage is limited at KARA to 1.6 MV [65].

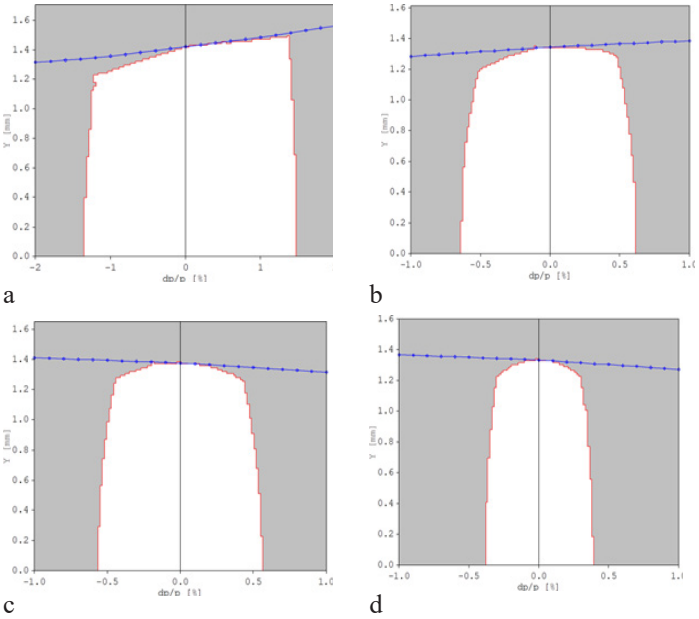

Figure 24: Momentum acceptance of the KARA lattice at different operation regimes. Scrapers reduce aperture of vacuum chamber to A_x=±13 mm in horizontal plane and A_y=±7 mm in vertical plane: (a) user mode with momentum compaction factor α_1=+9·10^{-3} and chromaticity ξ,x,y= +1/+1, (b) low-α mode with positive value of compaction factor α_1=+1.2·10^{-4} and chromaticity $\xi_{x,y}$= +1/+1; (c) negative compaction factor operation with α_1= -2·10-3 and negative chromaticity $\xi_{x,y}$= -0.5/-6; d) negative compaction factor regime with α_1= -7·10^{-3} and negative chromaticity $\xi_{x,y}$= -1/-6.

We simulated the dynamic aperture for off-momentum particles of the KARA storage ring at different operation regimes using the computer code OPA [58]. Scrapers at KARA reduce, for safety reason, the aperture of vacuum chamber to A_x=±13 mm in horizontal plane and A_y=±7 mm in vertical plane. In the 'user operation' regime with high momentum compaction factor α_1=+9·10^{-3}, the dispersion function is always positive and it is limited to 0.6 m (Fig.1). The dynamic aperture is opened and betatron oscillations are stable for particles with large momentum offset up to ±1.3% (Fig.24a). For lower positive compaction factors (α_1=+1·10^{-4}) the dispersion function is stretched from +1.44 m to -1.03 m (Fig.2), and the momentum acceptance is reduced to ±0.7% (Fig24b). At negative -α (α_1= -2·10^{-3}) the momentum acceptance is even less (±0.5%), see Fig24c. At high value of negative momentum compaction factor (α_1= -7·1$^{0-3}$) the beam motion is stable only for particles with small momentum deviations less than ±0.35% (Fig24d).

Possible conditions for α- buckets at KARA storage ring

We've estimated possible conditions to fill and store α- buckets at KARA taking into account limits imposed by the small momentum acceptance of a ring at lowα- operation. Variation of the main term of the compaction factor, α_1, was accomplished by tuning of the Q3 quadrupole family, see Fig.2. The rest of quadrupole families were adjusted to minimize deviation of betatron tunes during the squeezing procedure. At present, the KARA storage ring has only two sextupole families for chromaticity corrections, namely, horizontal (SH) and vertical (SV). In simulations we either reduce or increase the energy gap between RF and α- buckets by varying the strength of horizontal (SH) and vertical (SV) sextupole families. Some results are shown in Table 7.

The energy deviations of stable fixed points (α-buckets) were estimated in three different ways: the first by calculating the roots, (51), of the second order equation, (50), the second by calculating the roots, (63,64,65), of the third order equation, (49), and the third by tracking the orbit length for off-momentum particles (results of OPA tracking are shown in Table 7 in brackets). For estimation purposes, the free momentum independent term was zeroed (χ =0). Thus, the focus point of RF buckets corresponds here to the reference energy with zero momentum offset (δ=0).

Table 7: Parameters of α- buckets at KARA ring

α_1	α_2	α_3	$\delta\%_2$ (OPA-5th order)	$\delta\%_3$ (OPA-5th	$\delta\%_1$ (OPA-5th	chroma ξx,y	SH/SV×L^{-2} m
+9.7·10^{-3}	-8.8·10^{-3}	-0.96	-10.5(-9.3)	+9.6 (+7.5)	0	+1/+1	4.6/-3.3
+1.0·10-4	+7.13·10^{-3}	-0.278	-1.04 (-1.0)	+3.6 (3.6)	0	+1.37/+1.5	2.68/-2.06
+1.0·10^{-4}	+1.37·10^{-2}	-0.259	-0.68 (-0.67)	+5.9 (--)	0	+1/+1	2.6/-2.0
+1.0·10^{-4}	+3.26·10^{-2}	-0.274	-0.31 (-0.312)	+12 (--)	0	0 / 0	2.6/-1.86
-1.4·10^{-4}	-1.64·10^{-2}	-0.258	-1.01 (-1.02)	0	-5.3 (-2.7)	+0.9/+1.4	3/-2.27
-1.4·10^{-4}	-1.88·10^{-2}	-0.25	-0.83 (-0.85)	0	-6.7 (-3.3)	+1/+1	3/-2.25
-1.4·10^{-4}	-2.09·10^{-2}	-0.233	-0.72 (-0.73)	0	-8.3 (-3.8)	+1.2/+0.48	3/-2.213
-1.4·10^{-4}	-2.91·10^{-2}	-0.16	-0.49 (-0.49)	0	-17 (-5.8)	+1.7/-1.95	3/-2.044
-1.4·10^{-4}	+1.5·10^{-2}	-0.102	+0.99 (+1)	0	13.7	-0.6/-2.6	2.6/-1.814
-1.4·10^{-4}	+2.03·10^{-2}	-0.177	+0.73 (+0.73)	0	10.8	-1/-1	2.6/-1.92
-1.4·10^{-4}	+3·10^{-2}	-0.316	+0.48 (+0.48)	0	9.15	-1.6/+1.7	2.59/-2.1
-1.1·10^{-3}	+0.17	-2.36	+6.5(--)	0	+0.72(+0.72)	-8/-8	1.2/-0.8
-2.0·10^{-3}	+0.336	-9	+3(--)	0	+0.74(+0.74)	-14/-12	0/0

Images of RF and α-buckets in longitudinal phase space (ϕ, δ) are shown in Fig.25 for chosen values of low compaction factor terms α_1=1.0·10^{-4}, α_2= 7·10^{-3} and α_3= -0.278. RF bucket corresponds to reference energy (δ_1=0) while α-buckets are shifted in energy at (δ_2= +3.6%) and (δ_3=-1.0%). α-buckets are displaced in RF phase with respect to RF bucket at π.

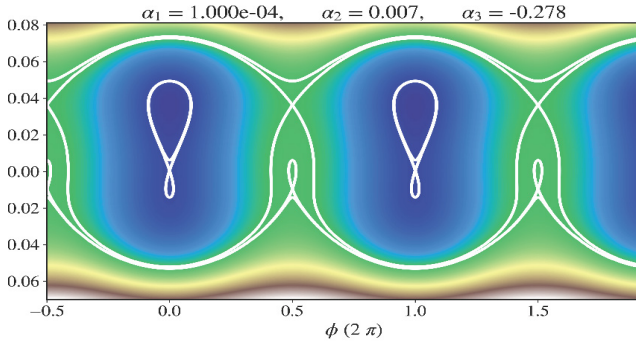

Figure 25: Images of RF and α-buckets in longitudinal phase space (ϕ, δ) for chosen values of low compaction factor terms α_1=1.0·10^{-4}, α_2= 7·10^{-3} and α_3= -0.278. RF bucket corresponds to reference energy (δ_1=0) while α-buckets are shifted in energy at (δ_2=+3.6%) and (δ_3=+1.0%). α-buckets are displaced in RF phase with respect to RF bucket at π. (Courtesy of A.-S. Müller).

Simulations of beam orbit lengthening by computer tracking reveals the fact that at large momentum deviations one should use a Polynomial of higher than three orders so as to fit a tracking curve. In Figure 26a the orbit length deviation is shown for the low negative-α mode. At small momentum offsets the "cubic parabola", described by third order equations (21) and (22), fits well to the orbit lengthening as a function of energy deviation. Three leading terms of momentum compaction factor α1= -1.4•10^{-4}, α2= -1.88•10^{-2} and α3= -0.25 were used. At a large momentum offset, the 5th order Polynomial should be applied to fit the pattern of the orbit length deviation

$$\Delta L = L_0 (\alpha_5\delta^4+\alpha_4\delta^3+\alpha_3\delta^2+\alpha_2\delta+\alpha_1)\,\delta \qquad (90)$$

The momentum compaction function described by the expression inside the brackets of equation (90) is shown in Figure 26b. The RF buckets with a first term α = -1.4•10^{-4}, are centered around a reference orbit with δ_3=0. Two nodes, where ΔL(δ) and α(δ) curves cross zero, define the position of stable fixed points with momentum offsets δ_2 = -0.85% and δ_1= -3.3%. The Energy gap between RF and α-buckets was estimated for the same conditions with the second and third order equations as δ_2 = -0.83% and δ_1= -6.7%. One can explain this discrepancy between the roots of the analytical expressions and that of those from the beam tracking by a contribution of higher order Polynomial terms at large momentum offsets (δ>2%). For practical use for storage rings with limited momentum acceptance, one should consider only small energy deviations; particularly we are restricted at KARA to δ≤1%. With these conditions the Polynomial of the third order fits the tracking curves with good accuracy. Expected "candidates" to fill and store α-buckets at the KARA storage ring are highlighted in bold in Table 7. For small momentum offsets, roots of analytical equations based on third order Polynomials (20), (21), and results of computer tracking, are very close to each other. One should emphasize that for any specified conditions presented in Table 7 only one stable α-bucket might be stored at KARA in addition to the standard RF bucket.

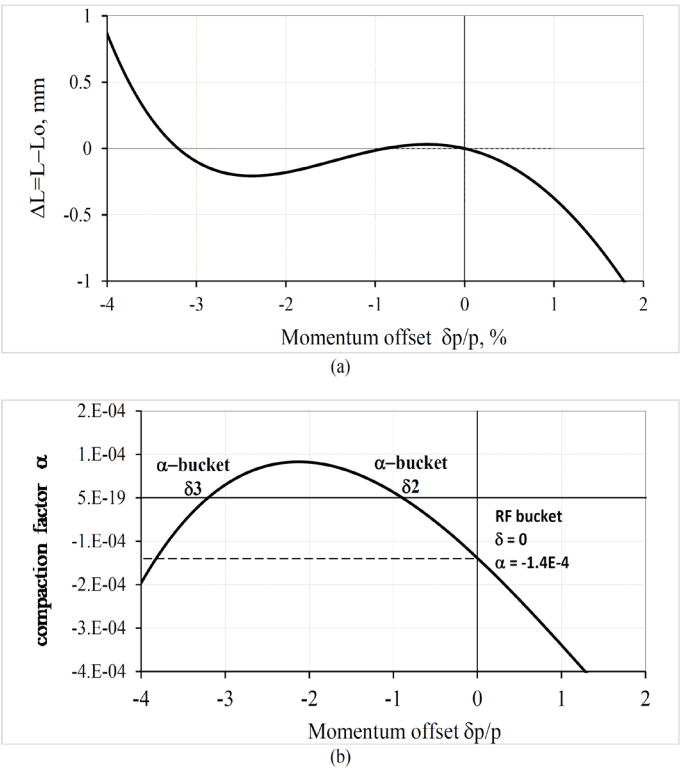

Figure 26: Beam orbit lengthening as a function of energy deviation: (a) off-momentum orbit length deviation from the reference orbit is described by the Polynomial of 5th order; (b) momentum compaction factor as function of momentum offset. While a stable fixed point with α_1= -1.4•10-4 corresponds to a RF bucket at δ=0, two other points, where α crosses zero, define the position of α-buckets with momentum offset δ_2 = -0.85 % and δ_1= -3.3 %

Energy offset of α-buckets at low positive compaction factor of the KARA storage ring

For positive values of the momentum compaction factor (α_1>0), the signs of the third and first terms are different, the curvature of momentum compaction function is negative and three real roots exist (63, 64, 65). As was expected, at high values of momentum compaction factor α_1=+9•10^{-3}, the energy offsets of the stable fixed points, (±10%), well exceeds the momentum acceptance of the ring (±1%). Therefore, only RF buckets can be stored while in the 'user operation' regime of KARA.

Short bunch operation at 1.3 GeV and low positive compaction factor α_1=+1•10^{-4}, is another routine regime of the KARA storage ring. This mode is used for studies of beam bursting effects caused by coherent synchrotron radiation in the THz frequency range [66, 67].

In this mode, one fills in and realizes simultaneous circulation of RF and α-buckets at a positive low-α regime, by adjusting the energy gap between RF and α-buckets so as to fit both beams into the ring momentum acceptance (Figure 27). For this, we slightly

decrease the strengths of SF and SD sextupole families, and reduce horizontal and vertical chromaticity from ξX,Y= +1.4/+1.5 down to ξX,Y= 0/0, see Table 7. As a consequence, the value of the second term of compaction factor grows from α_2=+7•10^{-3} (curve 1 in blue) up to α_2=+3.3•10^{-2} (curve 3 in red) and the slope of compaction factor curve α(δ) is increased. This results in the orbit lengthening curve, ΔL(δ), as well as the momentum compaction factor curve, α(δ), crossing

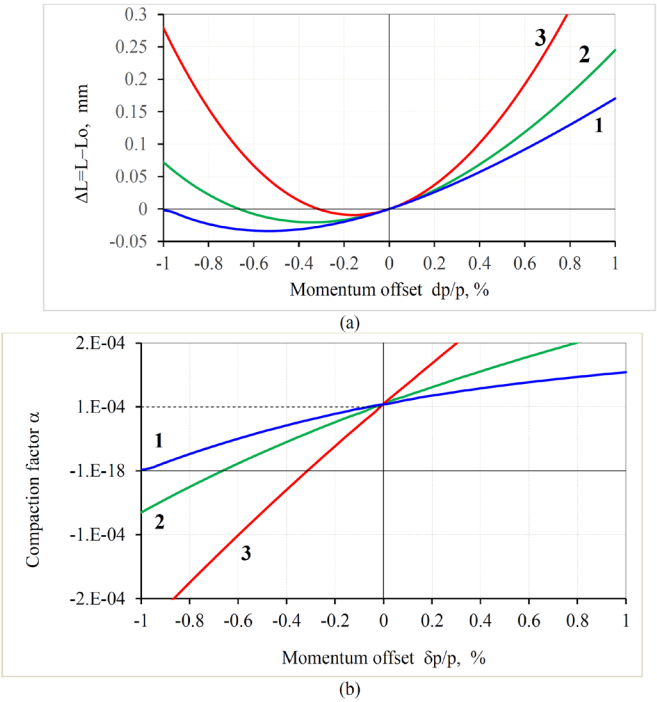

Figure 27: Reduction of the momentum offset of α-buckets with respect to the energy of the reference orbit at low-α mode with α_1=+1•10^{-4} by variation of second term of momentum compaction factor: (a) orbit lengthening as a function of momentum offset; (b) compaction factor vs energy deviation. Curve 1 (blue) corresponds to second term α_2=+7.13•10^{-3}, curve 2 (green) - α_2=+1.37•10^{-2} and curve 3 (red) - α_2=+3.26•10^{-2}.

The zero axis (ΔL=0) and (α=0) at smaller values of energy offset (δ) (Figure 27a, b). The energy gap between RF and α-buckets, shown in Figure 27, is reduced in absolute value from 1% down to 0.3%. One can capture both beams simultaneously providing the momentum offset between RF and α-buckets fits to the KARA storage ring acceptance at low-α.

In Figure 28 one can see the expected separation between two beams (RF and α-buckets) simultaneously stored in the KARA storage ring during low-α operation. The axis of Figure 28 is vertical (Y) and horizontal (X) beam positions. Bunches at 0.5 GeV and 1.3 GeV are split in the vertical plane for clarity. Dispersion is negative D= -1 m at the observation point (middle of long straight section). The first term of the momentum compaction factor α_1=+1•10^{-4} was chosen from estimations. It was assumed that the second term would reduce to α_2=+7•10^{-3} and the momentum offset between RF and α-buckets is 1%. In the middle of long straight section, the horizontal size of the low current 0.5 GeV beam at equilibrium is estimated as σx=0.7 mm (rms). The beam width is increased to σ_x=1.2 mm (rms) at 1.3 GeV because the natural momentum spread grows almost three times from σ_E=+1.8•10^{-4} at 0.5 GeV to σ_E=+4.7•10^{-4} at 1.3 GeV. The blue contour line depicts the projection of the vacuum chamber at the observation point. For the dynamic aperture, shown as a red contour line, together with this momentum acceptance, is sufficient to store both beams.

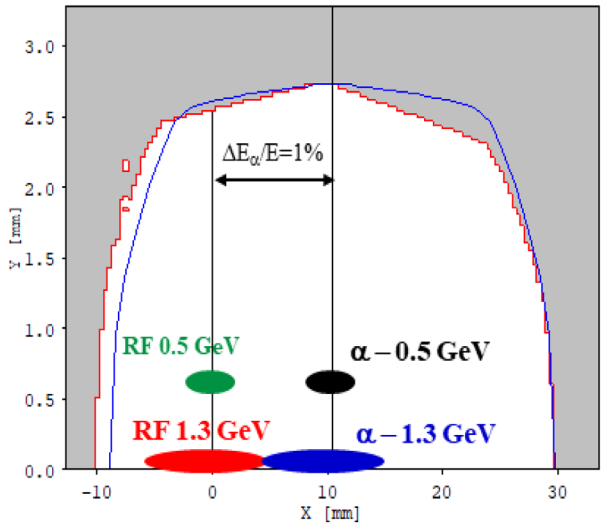

Figure 28: Expected images of RF and α-buckets to be simultaneously stored at KARA during low-α operation where the first term of momentum compaction factor is α_1=+1•10-4. Bunches at 0.5 and 1.3 GeV are split in the vertical plane for clarity. Dispersion D = -1m at observation point. It was assumed that momentum offset between RF and α-buckets is ~1%.

Positive low-α mode in presence of orbit errors

We simulated the energy offset of both RF and α-buckets at different values of orbit misalignments, associated with COD errors, by calculating roots (63, 64, 65) of the third order equation (49) where the free term (χ) has been varied, see Figure 29. The compaction factor was evaluated using the first term α_1=+1•10^{-4} and with the same starting conditions from Table 7 and Figure 27. In Figure 29 curves (1) and (1-α), both marked in blue, represent RF and α-buckets with the second term α_2=+7.13•10^{-3}, while curves (2) and (2-α) both marked in green, represent RF and α-buckets with α_2=+1.37•10^{-2} and curves (3) and (3-α) both marked in red, represent RF and α-buckets with α_2=+3.26•10^{-2}.

Initially on-momentum RF buckets (δ_1=0) are progressively off-centered from the reference orbit because the momentum independent term of relative orbit lengthening, (χ), grows from a low level of orbit errors (χ<10^{-9}) to large errors of (χ>1•10^{-7}); negative energy offset of α-buckets is reduced in absolute value at high levels of orbit errors.

For an initially small energy gap between RF and α-buckets (δ = 0.3%) it seems not to be possible to capture both beams simultaneously if the relative momentum independent term would exceed (χ>5•10^{-8}). According to estimations, see Figure 3, one should carefully center the beam and reduce orbit oscillations to less than 1 mm in order to limit relative free term to an acceptable level of (χ<5•10^{-8}). Precise adjustment of sextupole strength to limit the second term of momentum compaction factor within a small range

between 7•10-3< α2<1•10-2 should allow to capture both beams simultaneously when the energy gap between RF and α-buckets is large enough to split both beams in space but still fit to a ring acceptance (0.6%<δ<1%).

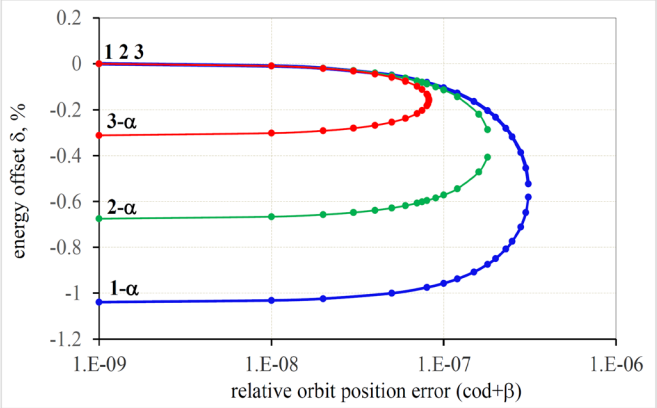

Figure 29: Energy offsets of α-buckets in the presence of momentum independent coherent orbit errors (χ). Positive low- α optics of the KARA storage ring with first term α_1=+1•10^{-4} was chosen as an example. Curves marked in blue represent RF (1) and α-buckets (1-α) with second term α_2=+7.13•10^{-3}, curves marked in green - RF (2) and α-buckets (2- α) with α_2=+1.37•10^{-2} and curves marked in red - RF (3) and α-buckets (3- α) with α_2=+3.26•10^{-2}. The on-momentum RF buckets are progressively off-centered from reference orbit (δ_1=0) at low level of COD errors to different energy offsets while momentum independent term of relative orbit lengthening (χ) grows from low to high values. Negative energy offsets of α-buckets are reduced in absolute value at high level of COD errors.

Momentum acceptance at positive low-α operation mode of the KARA storage ring

The synchrotron frequency, (FS), as a function of momentum offset, was estimated for positive low-α optics of the KARA storage ring. Equation (43) was applied to define dependence of (FS) up to the second order in momentum deviation (δ_2), see Figure 30. The following parameters have been chosen: beam energy is 1.3 GeV, RF voltage - 700 kV, RF frequency-500 MHz, RF harmonic number - 184 and the first term of momentum compaction factor is α_1=+1•10^{-4}. Figure 30 plots the following: Blue (1) and dashed blue (2) curves represent RF and α-buckets with the second term α_2=7.1•10^{-3}, curve (3) in green represents RF buckets with α_2=+1.4•10^{-2} and curve (4) in red represents RF buckets with α_2=+3.26•10^{-2}. Furthermore, the black dashed curve (5) corresponds to low-α optics with a reduced second order term α_2=+7•10^{-4}. As was discussed in previous sections, at certain conditions the criterion for zero synchrotron tune (FS=0) might be considered as the lowest limit imposed on the momentum acceptance of a ring. For all cases described in Figure 30 the maximum momentum offset, defined by condition of (FS=0), is approximately 2 times less than the limits imposed by the energy gap between RF and α-buckets. This Ratio is slightly higher than theoretical prediction of √3, because the second term, α_2, is not negligible and the synchrotron tune drops to zero even faster.

For example, with a second term at α_2=7.13•10^{-3}, the momentum acceptance is limited by synchrotron tune to ≈0.55% (curve 1 in Figure 30) while the energy gap between RF and α-buckets is δ_2=1% (curve 1 in Figure 27). With the second term at α_2=1.37•10^{-2}, the maximum beam energy deviation is limited by synchrotron tune to ≈0.35% (curve 3 in Figure 30), while the energy gap between RF and α-buckets is δ_2=0.67% (curve 2 in Figure 27). For a high value of the second term α_2=+3.26•10^{-2}, the synchrotron tune acceptance is reduced to 0.16%, even though the gap is δ_2=0.31%. The energy spread of the KARA beam at an injection energy of 500 MeV is σ_E=1.8•10^{-4} (Table 6). It is still possible to store the beam with this reduced momentum acceptance of a ring, but the life-time might be unacceptably small.

It is obvious that minimization of the second term of the momentum compaction factor to the level of α_2<10^{-3} would allow to increase the momentum acceptance and improve life-time during low-α experiments, see curve (5) in Figure 30. Unfortunately, the energy gap between RF and α-buckets for a very small second term α_2=+7•10^{-4} is equal to δ_1= -1.8% and δ_2=+2.1% i.e. well beyond the KARA lattice limits ±0.7% (Figure 24b). Therefore, only α-buckets can be stored with low positive compaction factors with a first term α_1=+1•10^{-4} and positive second term ranging between α_2≥+5•10^{-3} and α_2≤+3•10^{-2}.

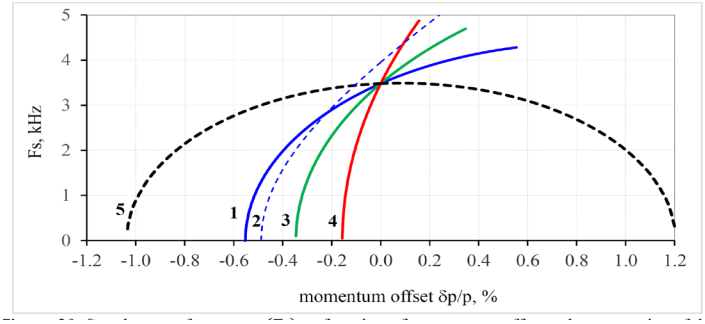

Figure 30: Synchrotron frequency (**FS**) as function of momentum offset at low-α optics of the KARA storage ring. The first term of the momentum compaction factor is α_1=1×10$^{-4.}$ **Blue** (1) and **blue** dashed (2) curves represent RF and α-buckets with second term α_2=+7.13•10^{-3}, **green** (3) curve - RF bucket with α_2=+1.37•10^{-2} and **red** (4) curve - RF bucket with α_2=+3.26•10^{-2}. **Black** dashed curve (5) illustrates dependence of synchrotron tune on energy deviation for a beam with third term α_3= -0.278and reduced second term α_2=+7•10^{-4}.

Estimation of life-time at low-α operation

When in a KARA low-α operation mode, the RF bucket height, see equation (86), exceeds ±13% and cannot limit the life-time of a beam. At certain conditions, namely, at low-α operation with first term α_1=+1•10^{-4}, the momentum acceptance of KARA is limited by the ring lattice to ±0.7% because of the high span of the dispersion function (Figure 24b). Moreover, the momentum acceptance is further reduced by high order terms of momentum compaction factor because of the drop of synchrotron tune to FS=0, see equation (89) and Figure 30. Condition FS=0 might be applied as a figure of merit in order to estimate the life-time of a beam.

Momentum acceptance as function of second term α2 is shown in Figure 31a. Increasing of the second term allows to reduce the energy gap between RF and α-buckets and capture both beams

(Figure 27), but at the expense of a sharp drop of acceptable energy spread, especially at large values of the second term α2≥10-2 (Figure 31a). While momentum acceptance is reduced the life-time drops.

The life-time of electrons in storage rings at moderate beam energies, (E~1 GeV) and high beam current per bunch (~1mA/bunch), strongly depends on loss rate due to the Touschek effect [46]. The Touschek life-time [47] might be estimated by the following equation

$$\tau_T = 8\pi\gamma^2 \frac{(\sigma_x \cdot \sigma_y \cdot \sigma_l)}{r_e^2 c \cdot n_e} (MA_{min})^3 \frac{1}{D(\zeta)} \quad , \qquad (91)$$

where σ's are transverse and longitudinal beam sizes are rms values, r_e is the classical electron radius, n_e the total number of particles in the bunch, c the velocity of light and γ the relativistic factor. The parameter, Momentum Acceptance $(MA)_{min}$, is a minimum of physical, dynamical, RF or synchrotron tune acceptances. The variable ζ depends on the square of momentum acceptance

$$\zeta = (MA_{min})^2 \left(\frac{\beta_x}{\gamma \cdot \sigma_x}\right)^2 \qquad (92)$$

and term D(ζ) is approximated by expression

$$D(\zeta) \sim \sqrt{\zeta}\,(-\ln(1.78\zeta - 1.5)) \qquad (93)$$

The Touschek life-time is inversely proportional to the bunch current, $\tau_\tau \sim ne^{-1}$, and it is improved when the momentum acceptance is increased $\tau_\tau \sim (MA_{min})$.

We've estimated the life-time for a 1.3 GeV electron beam as function of the second term of the momentum compaction factor (α_2), see Figure 31b. The low-α operation regime, with the first term $\alpha_1 = +1 \cdot 10^{-4}$, was chosen for our simulations. For each value of (α_2) we've estimated a corresponding limit on momentum deviation implied by the synchrotron tune, see Figure 31a, and calculated a life-time by the OPA tracking code. The code does not include an option to vary the momentum acceptance of a ring by changing the high order terms of the compaction factor, but does include the dependence of the momentum acceptance on amplitude of RF voltage, see equation (86). Thus, we've precisely adjusted the RF voltage in the OPA tracking subroutine "Touschek Lifetime" in order to fit to the desired value of momentum acceptance and estimated life-time.

Curve 1 (blue) and curve 2 (red) in Figure 31b correspond to expected life-time at low (0.1 mA/b) and high (1 mA/b) bunch currents. As predicted, the life-time drops significantly with an increase in the second term of the compaction factor. At high values of $\alpha_2 > 0.015$, the momentum acceptance is reduced to <0.3% and the beam might be lost, which is in good agreement with MLS experimental evaluations of life-time (Figure 17) and its theoretical interpretation (Figure 18, 19). Momentum acceptance of α-buckets defined by the synchrotron tune, FS, was estimated from curve (2) in Figure 30 and it is marked by a black square in Figure 31a. In Figure 31b the life-time of α-buckets is marked by a blue square for low bunch current and by a red square for high bunch current.

The amplitude of the RF voltage in our simulations was significantly reduced to ~50 kV in order to fit small values of momentum acceptance between 0.2% and 1%. As a consequence, zero current bunch length σl defined by expression [12, 13].

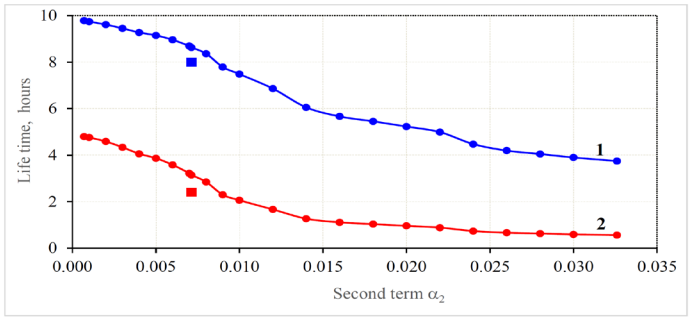

(b)

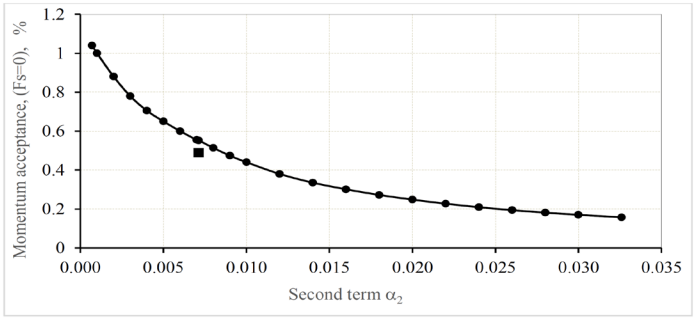

(a)

Figure 31: The momentum acceptance (a) and life-time (b) of KARA beam as a function of the second order term of the momentum compaction factor (α_2). Low-α operation mode with the first term $\alpha_1 = 10^{-4}$, the beam energy 1.3 GeV, average pressure 10^{-9} tor and RF frequency 500 MHz were chosen for estimations purposes. Curve 1 (**blue**) and curve 2 (**red**) correspond to expected life-time at low (0.1 mA/bunch) and high (1 mA/bunch) bunch current. Momentum acceptance of α-buckets was taken from curve (2) in Figure 26 and it is marked by a black square in (a). Life-time of α-buckets is marked by a **blue** and a **red** square in (b).

$$\sigma_l = L_0 \beta_0 \delta_p \sqrt{\frac{E_0 \cdot \alpha_1}{2\pi \cdot h_{RF} e U_{RF}(-\cos\varphi_s)}} \qquad (94)$$

was artificially increased in our simulations, and additional growth of Touschek loss rate due to bunch shortening was neglected. At high bunch current and low-α optics, when bunches are squeezed, one could expect greater beam losses and shorter life-time than the one shown in Figure 31b. In practice, during low/negative-α injection at 0.5 GeV, the RF voltage amplitude was decreased from 300 kV to 50 kV in order to increase bunch length, reduce Touschek loss rate and improve life-time to an acceptable level of 1.5 to 2 hours [16].

When the amplitude of the RF voltage is sufficiently high (~700 kV at 1.3 GeV), the total momentum acceptance is fixed by the ring lattice, and limited by a high span of the dispersion function to ±1%. The life-time of a beam with dominant Touschek effect depends on the density of particles in the bunch. Bunch length is decreased for a low momentum compaction factor α_1, see equation (94). In addition, by increasing the RF voltage, one squeezes bunches further down and reduces the bunch length σ_l. When

bunch density is increased, the Touschek loss rate grows and life-time is reduced – in contrary to the situation when life-time is improved with increasing of RF voltage.

α-buckets at negative momentum compaction factor of KARA storage ring

Few operation modes with negative momentum compaction factors were realized recently at KARA [16]. To build up the negative-α optics one should strongly stretch the dispersion function, see Figure 2, where the ring lattice with a negative compaction factor $\alpha 1 = -2 \cdot 10^{-3}$ is shown. With this operation regime of KARA, the span of the dispersion function grows from $D_{min} = -1.1$ m to $D_{nax} = -1.6$ m in order for the negative contribution to exceed the positive one inside bending magnets.

Possible options to fill in α-buckets at negative compaction factor

We've considered and analyzed a few possible options to generate α-buckets with a negative compaction factor. Namely,

- α-buckets at negative low-α mode with first term $\alpha_1 = -1.4 \cdot 10^{-4}$ and negative second terms $\alpha_2 < 0$
- α-buckets at negative low-α mode with first term $\alpha_1 = -1.4 \cdot 10^{-4}$ and positive second terms $\alpha_2 > 0$
- α-buckets at negative -α mode with first terms ranging from $\alpha_1 = -1 \cdot 10\text{-}3$ to $\alpha_1 = -2 \cdot 10^{-3}$ and positive second terms $\alpha_2 > 0$

The third term of the momentum compaction factor of the KARA lattice is less than zero ($\alpha_3 < 0$), see Table 7. Thus, for a positive values $\alpha_1 > 0$, as well as for negative values, $\alpha_1 < 0$, the curvature of compaction factor as a function of momentum offset $\alpha(\delta)$ is negative. By adjusting SH and SV sextupole families for zero longitudinal chromaticity $\xi_l \sim 0$, one can explore an opportunity to reduce the absolute value of the negative compaction factor down to the level of 10-5. This procedure involves the minimization of the second order term α2. As a consequence, the α-buckets cannot be built at very low negative compaction factors unless dedicated octupole lenses are installed at KARA in order to reverse the curvature of the momentum compaction factor.

Strong limitations exist when reducing a positive value of momentum compaction factor to a low level of <10-4 because of the natural curvature of the momentum compaction factor is still negative, see Table 7. At very low values of the first term $\alpha 1 \approx 10\text{-}5$, the momentum acceptance is so small that particles on the periphery of the momentum distribution of a beam will be outside of the area of stable motion, and the beam will be lost.

The same is true for low negative compaction factors ($\alpha 1 = -10^{-4}$), one can find a proper combination of the second $-\alpha_2$ and third -α3 order terms, and build up the ring optics with simultaneous RF and α-buckets, see Figure 32. Adjustment of α2 could be realized by a variation of strengths of the existing sextupole families SH and SV, see Table 7.

At KARA, the signs of the first ($\alpha_1 < 0$) and the third ($\alpha_3 < 0$) terms are the same at a negative compaction factor; the curvature of the momentum compaction function, $\alpha(\delta)$, is negative, and three real roots, (63, 64, 65), might exist only when the absolute value of the second term (α_2) is sufficiently large, and condition (52) is satisfied. For all described cases the energy offset of one real root well exceeds the physical dimensions of the KARA chamber (3%) and the beam cannot be stored in α-buckets, see Table 7. The difference between 3rd order Polynomial and the 5th order orbit tracking is essential, but roots with large momentum offset are excluded from further consideration. Meanwhile, the energy gap between two other stable fixed points is fitted to the ring acceptance (±0.5% and ±0.7%) i.e. RF and α-buckets can be stored simultaneously. At small momentum offsets (δ<1%), difference between roots of 3rd order Polynomial and 5th order orbit tracking is negligible.

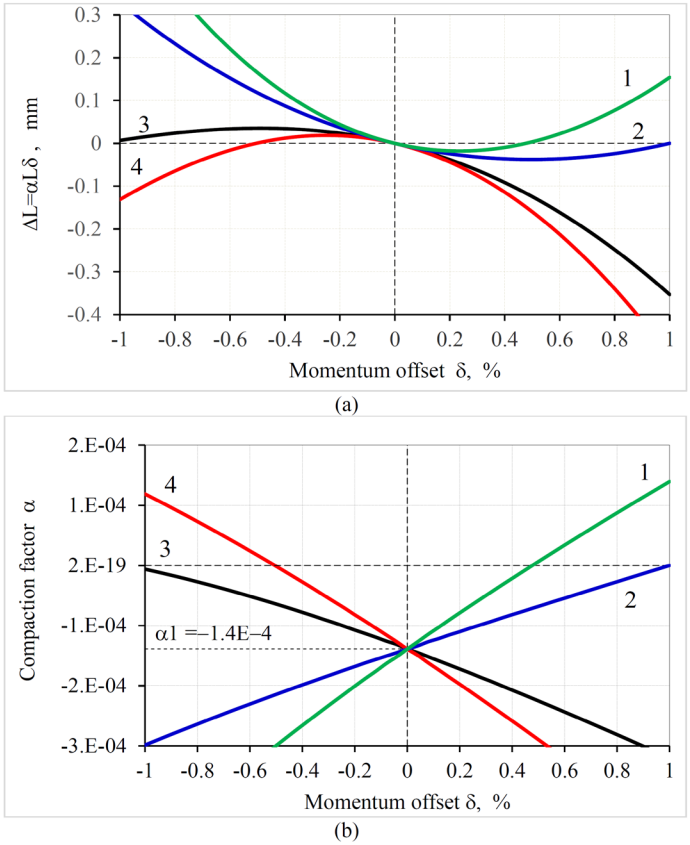

Figure 32: Energy gap between RF and α-buckets at negative low-α mode with first term $\alpha_1 = -1.4 \cdot 10^{-4}$ as a function of the second term of momentum compaction factor: (a) Variation of orbit lengthening with momentum offset; (b) compaction factor as function of energy gap. Curves 1 (**green**) and 2 (**blue**) correspond to positive slope with second terms $\alpha_2 = +3 \cdot 10^{-2}$ and $\alpha_2 = +1.5 \cdot 10^{-2}$, curves 3 (**black**) and 4 (**red**) - negative slope with second terms $\alpha_2 = -1.6 \cdot 10^{-2}$ and $\alpha_2 = -2.9 \cdot 10^{-2}$.

Stable fixed points are fitted to the KARA storage ring acceptance and equations (63, 64, 65) can be applied for our studies.

Variation of energy gaps between RF and α-buckets with negative low-α optics, and the first term $\alpha_1 = -1.4 \cdot 10\text{-}4$ was simulated by changing the second term of the momentum compaction factor, see Figure 32. The orbit lengthening and momentum compaction factor, as a function of energy deviation, are presented in Figure 32a and Figure 32b correspondingly. Curves 1 (green) and 2 (blue) represent a positive slope with second terms $\alpha_2 = +3 \cdot 10^{-2}$ and $\alpha_2 = +1.5 \cdot 10^{-2}$, while curves 3 (black) and 4 (red) represent a negative slope with second terms $\alpha_2 = -1.6 \cdot 10^{-2}$ and $\alpha_2 = -2.9 \cdot 10^{-2}$. For

both, positive and negative slopes, the momentum offset between RF and α-buckets is reduced, while the absolute value of the second term, α2, is increased.

At a positive slope (α_2>0), one can increase the energy gap between RF and α-buckets from +0.3% to +0.7% by reduction of the strength of vertical sextupoles SD.

KARA experiments indicate strong instabilities during beam injection into negative-α optics with positive chromaticity ξX,Y>0. However, the beam was stabilized when the strength of sextupoles has been reduced for negative chromaticity.

During the adjustment procedure at negative-α optics with positive second term α_2>0, both horizontal ξX, and vertical ξY chromaticities are negative (ξX,Y<0), and the beam should be stable.

At low negative-α optics, and with a negative slope of the second term (α_2<0), one can broaden the energy gap between RF and α-buckets from -0.3% to -0.7% by increasing the strength of vertical sextupoles SD (Table 7). Unfortunately, during the adjustment procedure of the negative second term, α_2<0, the horizontal ξX and vertical ξY chromaticity are positive ξX,Y>0 and beam accumulation might be harmed by instabilities.

Negative α-buckets with non-negligible momentum independent free term (χ≠-0)

Energy deviation of RF and α-buckets in the presence of momentum independent coherent orbit errors (χ) was estimated for negative values of momentum compaction factor. In particular, we considered the case of a low first term α_1= -1.4•10^{-4}; the energy gap between RF and α-buckets is shown in Figure 33 as a function of the relative term (χ). Curves 1 and 1-α (blue) represent RF and α-buckets with the second terms α_2= -1.6•10^{-2}, curves 2 and 2-α (green) represent RF and α-buckets with α_2= -2.1•10^{-2} and curves 3 and 3-α (red) represent RF and α-buckets with α_2= -2.9•10^{-2}. Initially, on-momentum RF buckets are progressively off-centered from the reference orbit (δ_1=0) at low level of COD errors (χ≤10-8) with respect to energy offsets, while relative orbit lengthening grows to a high error level of (χ≥3•10^{-7}).

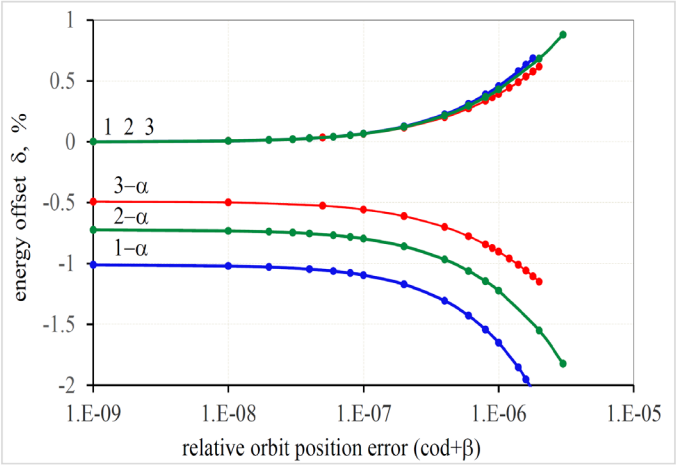

Figure 33: Energy offset of RF and α-buckets at low negative momentum compaction factor α_1= -1.4•10^{-4} and negative second term in the presence of the momentum independent term (χ) associated with COD errors. Curves 1 and 1-α (**blue**) represent RF and α-buckets with second term α_2= -1.6•10^{-2}, curves 2 and 2-α (**green**) - RF and α-buckets with α_2= -2.1•10^{-2} and curves 3 and 3-α (**red**) - RF and α-buckets with α_2= -2.9•10^{-2}. Initially on-momentum RF buckets are progressively off-centered from reference orbit (δ_1=0) at low level of COD errors (χ≤10^{-8}) with respect to positive energy offsets while momentum independent term of relative orbit lengthening grows to high level (χ≥5•10^{-7}). Energy offset of α-buckets grows in absolute value at high error level.

In contrary to positive low-α optics (Figure 29), RF and α-buckets at negative compaction factor and negative second term (α_2<0) are diverged, while COD errors grow. Energy offsets of RF, as well as α-buckets, are increased in absolute value at high levels of COD errors, see curves 1, 2, 3 for RF buckets and curves 1-α, 2-α and 3-α for α-buckets in Figure 33.

There is no limit on the maximum allowable level of parameter (χ), and expression (72) is always satisfied. In this case RF and α-buckets still exist and are always separated at large (χ), but the energy gap between RF and α-buckets is increased and will exceed the momentum acceptance of the storage ring at a high level of COD errors. Orbit distortions at a level of (χ≤3•10-7) might be considered as a practical limit on 'beam off-centering' for a case of negative first and second terms.

In contrary to negative low-α optics (where (α_1<0) and a negative slope (α_2<0)), RF and α-buckets at a negative compaction factor (with (α_1<0) and a positive second term (α_2>0)) are converged while COD errors grow, see Figure 34.

Curves 1 and 1-α (blue) represent RF and α-buckets with the second terms α_2=+1.5•10^{-2}, curves 2 and 2-α (green) represent RF and α-buckets with α_2=+2.03•10^{-2} and curves 3 and 3-α (red) represent RF and α-buckets with α_2=+3•10^{-2}. Initial energy offsets of α-buckets are +1% (curve 1-α), +0.73% (curve 2-α) and +0.48% (curve 3-α). Similar to positive low-α optics (Figure 29), initially on-momentum RF buckets increase the momentum offset from a nominal energy, while COD errors grow to high level of (χ≥1•10^{-7}). Concurrently, for high level of COD errors, α-buckets reduce its positive energy gap with respect to the reference orbit, see curves 1-α, 2-α and 3-α at Figure 34. RF and α-buckets are converged and stability should be lost when both buckets will merge in energy.

One should consider that the operation of α-buckets with a negative second term should be more stable against orbit lengthening caused by beam trajectory misalignments. The limit imposed on relative COD errors at negative value of second term α_2<0 is (χ≤5•10^{-7}), see Figure 33 and it is reduced to (χ≤1•10^{-7}) for a positive slope of compaction factor, regardless of the sign of the first term α1, see Figure 33 and Figure 34.

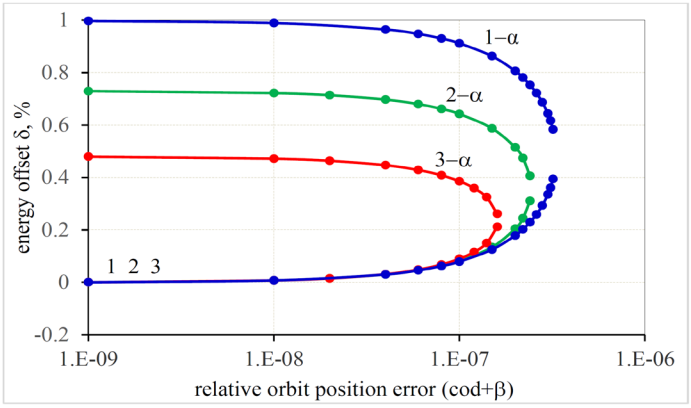

Figure 34: Energy offset of RF and α-buckets at low negative momentum compaction factor α_1= -1.4•10^{-4} and positive second term in presence of momentum independent COD errors (χ). Curves 1 and 1-α (**blue**) represent RF and α-buckets with second terms α_2=+1.5•10^{-2}, curves 2 and 2-α (**green**) - RF and α-buckets with α_2=+2.03•10^{-2} and curves 3 and 3-α (**red**) - RF and α-buckets with α_2=+3•10^{-2}. Initially on-momentum RF buckets are progressively off-centered from reference orbit towards positive energy offsets while momentum independent term of relative orbit lengthening grows to high level at (χ≥1•10^{-7}). Energy offset of α-buckets is decreased at high level of COD errors. RF and α-buckets are converged.

Synchrotron tune at negative compaction factor

We computed the dependence of synchrotron tune on the beam energy deviation with an objective to estimate the momentum acceptance of a ring with negative low-α optics. The synchrotron frequency as function of momentum offset, **FS(δ)**, in a negative low-α regime of the KARA storage ring is shown in Figure 35. The first term of the compaction factor was fixed to α_1= -1.4•10^{-4} for all curves presented. Curve (1), marked in **green**, represents the synchrotron tune for optics with a positive second term α_2=+3•10^{-2}, negative third term α_3= -0.316 and an energy gap between RF and α-buckets δ_1=0.48%. Curve (2), marked in **blue**, refers to the beam with α_2=+1.5•10^{-2}, α_3= -0.102 and δ_2=0.99%. Curve (3), marked in **black**, corresponds to the beam with a negative second term α_2= -1.6•10^{-2}, α_3= -0.258 and δ_3= -1.01% and curve (4), marked in red, represents a beam with a negative second term α_2= -2.9•10^{-2}, α_3= -0.16 and δ_3= -0.49%.

One can see that for any value of the second term of the momentum offset, where the synchrotron tune is approaching zero i.e. δ_{Fs}=0=±0.48%, as is for curves 2 and 3, as well as δ_{Fs}=0=±0.24% for curves 1 and 4, it is almost two times less than the energy offset of corresponding α-buckets i.e. $\delta_{\Delta L}$=0=±1% described by curves 2 and 3 as well as $\delta_{\Delta L}$=0=±0.48% for α-buckets described by curves 1 and 4.

By decreasing the energy gap between RF and α-buckets, for example from 0.7% down to 0.3%, one can better fit both beams to the dynamic aperture of a ring, but at an expense of reduced momentum acceptance and a drop of life-time. Our simulations of synchrotron tune as a function of the momentum offset reveal that the momentum acceptance for negative-α optics is not much different from those for positive low-α optics, compare Figure 30, 31a and Figure 35. We believe our estimations of life-time for RF and α-buckets at positive low-α optics (Figure 31b) might be applied as well for negative low-α optics.

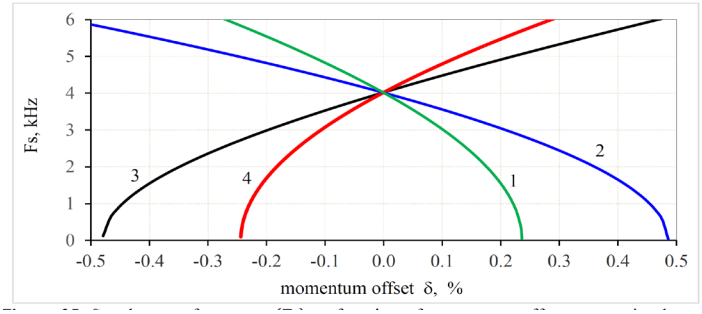

Figure 35: Synchrotron frequency (**FS**) as function of momentum offset at negative low-α optics of the KARA storage ring with first term α_1= -1.4•10^{-4}. **Green** (1) curve represents beam with positive second term α_2=+3•10^{-2}, negative third term α_3= -0.316 and energy gap between RF and α-buckets δ_1=0.48%; blue (2) curve - beam with α_2=+1.5•10^{-2}, α_3= -0.102 and δ_2=0.99%; black (3) curve - beam with negative second term α_2= -1.6-10^{-2}, α_3= -0.258 and δ_3= -1.01%; red (4) curve - beam with negative second term α_2= -2.9•10^{-2}, α_3= -0.16 and δ_3= -0.49%.

Conclusion

In this paper, consistent analysis of different experiments with low-α beams has been provided. High order terms of the momentum compaction factor, as well as a free momentum independent term describing relative orbit lengthening due to CODs and betatron motion, were included into equations of longitudinal motion. Solutions for three real roots of third order equations with a free term have been derived in a form suitable for analytical estimations and were applied for analytical studies of RF and α-buckets. Results of analytical studies based on second and third order equations were compared with high order computer tracking, and benchmarked against existing experiments at KARA, SOLEIL and MLS rings. Even though at large momentum offsets only the polynomial of fifth (and higher) order fits to the orbit lengthening and momentum compaction factor as functions of energy deviation, one can apply the equation of cubic parabola based on the Cardano equation for practical purposes at small energy gaps between RF and α-buckets in existing storage rings.

We showed that for certain conditions, strong dependence of the synchrotron tune on the energy offset might limit the momentum acceptance and life-time at low and negative-α operation.

The momentum independent term of orbit lengthening at the KARA storage ring caused by particle transverse excursions was estimated and taken into account. Based on good agreement between simulations and experimental data we expanded our studies to other rings and have used an example of KARA electron synchrotron to estimate possible conditions and constrains for α-buckets, beam life-time etc.

The authors are grateful to the operation, diagnostics, and power supply groups of KARA storage ring for their support during low and negative-α experiments.

References

1. AS Müller, M Scwarz (2016) Accelerator Based THz Radiation Sources" in book „Synchrotron Light Sources and free electron Lasers". Springer 83-118.
2. M Schmidt (2015) Time-Resolved Crystallography at X-ray Free Electron Lasers and Synchrotron Light Sources", Synchrotron Radiation News 28: 25-30.
3. JB Murphy, SL Kramer (2000) "First Observation of simultaneous Alpha Buckets in a Quasi-Isochronous Storage ring". Phys Rev Lett 84: 5516.
4. M Attal, P Brunelle, A Loulergue, A Nadji, L Nadolski, et al. (2013) "Dynamics of three simultaneously stored beams in a storage ring". Phys Rev STAB 16: 054001.
5. J Feikes, M von Hartrott, M Ries, P Schmid, G Wüstefeld (2011) "Metrology Light Source: The first electron storage ring optimized for generating coherent THz radiation". Phys Rev STAB 14: 030705.
6. M Ries, J Feikes, A Jankowiak, P Schmid, G Wüstefeld (2011) "Simultaneous long and short bunch operation in an electron storage ring – a hybrid mode based on nonlinear momentum compaction". Proc IPAC2011, San-Sebastian, Spain 2011: 945-947.
7. IPS Martin, G Rehm, C Thomas, R Bartolini (2011) "Experience with low-alpha lattice at the Diamond Light Source". Phys Rev STAB 14: 040705.
8. M Ries (2014) "Nonlinear Momentum Compaction and Coherent Synchrotron Radiation at the Metrology Light Source". PhD Thesis 2014: 120.
9. David AG Deacon (1981) "Basic Theory of the Isochronous Storage Ring Laser". Physics Reports (Phys. Letters) 76: 349-391.
10. J Le Duff (1994) "Longitudinal Beam Dynamics in Circular Accelerators". In Proceed. of 5th CERN Accelerator School-92, Finland 1994: 289-312.
11. H Wiedemann (2015) Particle Accelerator Physics. Fourth edition, Springer, Berlin, Heidelberg, Section 9: 4.
12. A Volskii (2014) Beam dynamics in high energy particle accelerators. Imperial College Press, London, UK 2014: 606.
13. AW Chao, K Hubert Mess, M Tigner, F Zimmermann (2013) Handbook of Accelerator Physics and Engineering- 2nd Edition. World Scientific 2013: 848.
14. SY Lee (2019) Accelerator Physics" 4th edition, https://doi.org/10.1142/11111.
15. P Schreiber, T Boltz, M Brosi, B Haerer, A Mochihashi, et al. (2019) Status of operation with negative momentum compaction at KARA. Proceed IPAC-19, Melbourne, Australia 2019: 878-881.
16. J-P Delahaye, J Jaeger (1986) "Variation of the dispersion function, momentum compaction factor, and damping partition numbers with particle energy deviations". Particle Accelerators 18: 183-201.
17. K-Y Ng (1998) "Quasi-isochronous buckets in storage rings". Nucl. Instr. & Methods A 404: 199-216.
18. J Bengtsson (1997) "The sextupole scheme for the Swiss Light Source (SLS): an analytical approach. SLS Note 9/97, PSI, Switzerland 57.
19. D Robin, E Forest, S Pellegrini, A Amiry (1993) "Quasi-isochronous storage rings". Phys Rev E 48: 2149-2156.
20. A Nadji, P Brunelle, G Flynn, MP Level, M Sommer, et al. (1996) "Quasi-isochronous experiments with the Super-ACO storage ring". Nucl Instr & Meth A 378: 376-382.
21. https://mathworld.wolfram.com/CubicFormula.html.
22. R V Churchill, J W Brown (2008) "Complex Variables and applications". McGraw-Hill Higher education. 8th edition 468.
23. https://www.encyclopediaofmath.org/index.php/Cardano_formula. B. L. Waerden, „Algebra" , 1–2 , Springer, (1967–1971). A. G. Kurosh "Higher algebra", MIR (1972)
24. H Klingbeil, U Laier, D Lens (2015) "Theoretical foundation of Synchrotron and Storage Ring RF systems". Springer 423.
25. I Bronshtein, K Semendyayev, G Musiol, H Mühlig (2007) "Handbook of Mathematics", 5th edition Springer-Verlag, Berlin, Heidelberg.
26. https://en.wikipedia.org/wiki/Discriminant, https://oeis.org/wiki/Cubic_formula.
27. EB Vinberg (2003) A course in algebra. American Mathematical Society, Providence, R.I, 2003: 511.
28. A Papash, E Blomley, J Gethmann, E Huttel, A-S Müller, et al. (2017) "High order magnetic field components and non-linear optics at the ANKA storage ring", Proc. IPAC-17, Copenhagen, Denmark 2017: 2586-2688.
29. A Papash, E Blomley, M Brosi, J Gethmann, B Kehrer, et al. (2018) Non-linear optics and low alpha operation at the storage ring KARA at KIT", Proc. IPAC-18, Vancouver, Canada 2018: 4235-4238.
30. A Papash, E Blomley, T Boltz, M Brosi, E Bründermann, et al. (2019) New operation regimes at the storage ring KARA at KIT", Proc. IPAC-19, Melbourne, Australia 2019: 1422-1425.
31. B Holzer (2017) Beam Dynamics in Synchrotrons. CERN Yellow Report CERN 2017-004-SP 2017: 253-284.
32. H Moser, D Einfeld, R Steininger (1995) ANKA Synchrotronlichtquelle für Mikrofertigung und Analytik. Design report, Forschungzentrum Karlsruhe.
33. M Zisman (1987) ZAP and its application to the optimization of synchrotron light source parameters", Proc. IEEE Part. Acc. Conf.-87, Washington, USA 1987: 991-995.
34. H Hama, S Takano, G Isoyama (1993) Control of the bunch length on an electron storage ring. Nucl. Instr. & Meth A 329: 29-36.
35. J Filhof, JC Besson, P Brunelle, M-E Couprie, J-C Denard, et al. (2006) Overview of the status of the SOLEIL project. Proc EPAC2006, Edinburg, Scotland 2006: 2723-2726.
36. R Klein, G Brandt, R Fliegauf, A Hoehl, R Müller, et al. (2008) Operation of the Metrological Light Source as a primary radiation source standard", Phys. Rev. ST Accel. Beams 11: 110701.
37. B Beckhoff, A Gottwald, R Klein, M Krumrey, R Müller, et al. (2009) A quarter century of metrology using synchrotron radiation by PTB in Berlin. Phys Status Solidi B 246: 1415-1434.
38. G Wuestefeld (2008) Short bunches in electron storage rings and coherent synchrotron radiation". Proc. EPAC08, Genova, Italy 2008: 26-30.
39. MJ Moravcsik, JM Sellen (1955) "Gas scattering in a strong focusing electron synchrotron". Rev Sci Instr 26: 1158.
40. JM Greenberg (1951) "Scattering losses in the Synchrotron". Rev Sci Instr 22: 293.
41. FR Elder, RV Langmuir, HC Pollock (1948) "Radiation from Electrons Accelerated in a Synchrotron". Phys Rev 74: 52.
42. H Wiedermann (1999) Beam Life Time "in: „Particle Accelerator Physics I "1999: 370-383.
43. GR Blumenthal, RJ Gould (1970) "Bremsstrahlung, Synchro-

tron Radiation, and Compton Scattering of High-energy Electrons Traversing Dilute Gases". Rev Mod Phys 42: 237.
44. M Martini, M Conte (1985) "Intra-beam scattering in the CERN Antiproton Accumulator". Proc Part Accelerators Conference 17: 1-10.
45. A Piwinski (1974) "Intrabeam scattering", Proc. 9th Int. Conf. on High energy Accelerators SLAC, USA 1974: 405-41.
46. J Le Duff (1985) "Current and current density limitations in existing electron storage rings". Nucl Instr Meth A 239: 83-101.
47. A Piwinski (1984) "Beam losses and lifetime", Proc. CERN Accelerator School, Gifsur-Yvette, Paris 1984: 432-462.
48. A Streun (1997) "Momentum acceptance and Touschek lifetime". SLS Note 18/97, PSI, Switz 1997: 12.
49. D Bjorken, SK Mtingwa (1989) "Intrabeam scattering". Particle Accelerators 13: 115-143.
50. J Le Duff (1989) "Single and multiple Touschek effects". Technical report CERN-89-01, CERN.
51. M Böge, A Streun (1999) "Beam life time studies for the SLS storage ring", Proc. Part. Accelerartor Conf.-99, New York, USA 1999: 2430-2432.
52. N Carmignani (2016) "Touschek Lifetime Studies and Optimization of the European Synchrotron Radiation Facility", Springer International Publishing Switzerland 2016: 102.
53. R Bartolini, C Abraham, M Apollonio, C Bailey, M Cox, et al. (1989) "Double-double bend achromat cell upgrade at the Diamond Light Source: From design to commissioning", Phys. Rev. Accel. Beams 21, 050701 (2018). M. Cornacchia, "Requirements and limitations on beam quality in synchrotron radiation sources", SLAC report, SLAC-PUB-5021, Stanford, USA 1989: 21.
54. A-S Müller, I Birkel, B Gasharoa, E Hutel, R Kubat, et al. (2005) "Far Infrared Coherent Synchrotron Edge Radiation at ANKA", in Proc. PAC-2005, Knoxwille, Tennessee, USA 2005: 2518-2520.
55. A-S Müller, A Ben Kalefa, I Birkel, E Huttel, F Perez, et al. (2005) Momentum Compaction Factor and Nonlinear Dispersion at the ANKA Storage Ring", in Proc. EPAC-2004, Lucerne, Switzerland 2004: 2005-2007.
56. T Bückle (2008) "Determination of the Radiation energy of the ANKA Storage ring by Means of Resonant Electron Spin Depolarization". Master Degree Thesis, Karlsruhe University, Germany 2008: 74.
57. Chang Cheng (2016) "Precise determination of the electron beam energy with Compton backscattered laser photons at ANKA", PhD Thesis, Karlsruhe University, Germany. https://publikationen.bibliothek.kit.edu/1000051914.
58. A Streun (2015) OPA Lattice Design Code, https://ados.web.psi.ch/opa/.
59. L Nadolski, G Abeillé, Y Abiven, P Alexandre, F Bouvet, et al. (2018) "SOLEIL Status Report", Proc. IPAC2018, Vancouver, Canada 2018: 4516-4519.
60. SC Leemann, M Sjöström, A Andersson (2018) First optics and beam dynamics studies on the MAX-IV 3 GeV storage ring". Nucl Instr and Meth A 883: 33-47.
61. S Krinsky, J Bengtsson, S Kramer (2006) "Consideration of a Double Bend Achromatic Lattice for NSLS-II". Proc EPAC06, Edinburg, UK 2006: 3487-3489.
62. "Lattice and accelerator physics" (2013) Chapter 6 of NSLS-II Conceptual design report 2013: 65.
63. A Streun, T Garvey, L Rivkin, V Schlott, T Schmidt, et al. (2018) "SLS-2 – the upgrade of the Swiss Light Source". Journal of Synchrotron Radiation 2018: 11.
64. E Jaeschke, S Khan, D Krämer, D Schirmer (1995) Status of the high brilliance synchro-tron radiation source BESSY-II. Proc PAC-95 Dallas USA 1995: 1411-1413.
65. P Raimondi (2016) "The ESRF low emittance upgrade". Proc IPAC-16, Busan, Korea 2016: 2023-2027.
66. D Einfeld, F Perez, S Voigt, M Bocciai, A Fabris, et al. (1998) "The ANKA RF cavities". Proc. EPAC-98, Stockholm, Sweden 1998: 1817-1819.
67. M Brosi, E Blomley, E Bründermann, M Caselle, B Kehrer, et al. (2017) "Studies of the Micro-Bunching Instability in Multi-Bunch Operation at the ANKA Storage Ring". Proc. IPAC-17, Copenhagen, Denmark 2017: 3645-3648.
68. M Brosi, J Steinmann, E Blomley, T Boltz, E Bründermann, et al. (2019) "Systematic studies of the microbunching instability at very low bunch charges". Phys Rev Accelerators and Beams 22: 020701.